Posted on 21 Nov 2022 — The copyright holder is the author/funder. All rights reserved. No reuse without permission. — https://doi.org/10.1002/essoar.10510964.1 — This a preprint and has not been peer reviewed. Data may be preliminary.

CO2 Dissolution Efficiency during Geological Carbon Sequestration (GCS) in Randomly Stratified formations

yufei wang[1], Daniel Fernandez Garcia[2], and Maarten W. Saaltink[3]

[1]Universitat Politècnica de Catalunya
[2]Technical University of Catalonia
[3]Department of Civil and Environmental Engineering, Universitat Politècnica de Catalunya (UPC)

November 21, 2022

Abstract

Geological Carbon Sequestration mitigates climate change by capturing and storing carbon emissions in deep geologic formations. Dissolution trapping is one mechanism by which CO2 can be trapped in a deep formation. However, heterogeneity can significantly influenced dissolution efficiency. This work addresses the injection of CO2 in perfectly stratified saline formations under uncertainty. Monte Carlo two-phase flow compositional simulations involving the dissolution of CO2 into brine and evaporation of water into the CO2-rich phase are presented. We systematically analyzed the interplay between heterogeneity and buoyant forces, which is shown to control the migration of the CO2 plume as well as the temporal evolution of dissolution efficiency. Results show that when buoyant forces are important, vertical segregation controls the overall behavior of CO2, diminishing the influence of small-scale heterogeneity on dissolution. However, when buoyant forces are relatively small compared to the degree of heterogeneity, CO2 migrates preferentially through high permeability layers and dissolution efficiency increases with heterogeneity due to the stretching of the CO2 plume that enhances mixing. As a result, in this situation, the upscaling of permeability leads to an underestimation of the dissolution efficiency. A review of field sites shows that dissolution is heterogeneity-controlled in most real systems. Knowing that most numerical models cannot afford to represent heterogeneity at an adequate scale, results indicate that dissolution efficiency can be typically underestimated by a factor close to 1.5.

CO_2 Dissolution Efficiency during Geological Carbon Sequestration (GCS) in Randomly Stratified formations

Yufei Wang[1,2] **Daniel Fernàndez-Garcia**[1,2] **Maarten W. Saaltink**[1,2]

[1]Dept. of Civil and Environmental Engineering, Universitat Politècnica de Catalunya, Jordi Girona 1-3, 08034 Barcelona, Spain
[2]Associated Unit: Hydrogeology Group (UPC-CSIC)

Key Points:

- Mont Carlo simulations of Geological CO_2 Sequestration (GCS) in randomly stratified porous media;
- Dissolution trapping plays an important role in GCS, representing around 20% of the injected CO_2;
- The interplay between heterogeneity and buoyant forces controls the behavior of CO_2 migration and dissolution efficiency;
- In heterogeneity-controlled systems, permeability stratification enhances CO_2 dissolution efficiency by stretching the interface between gas and brine phases;
- The upscaling of permeability can lead to an underestimation of the dissolution efficiency.

Corresponding author: Yufei Wang, yufei.wang@upc.edu

Abstract

Geological Carbon Sequestration mitigates climate change by capturing and storing carbon emissions in deep geologic formations. Dissolution trapping is one mechanism by which CO_2 can be trapped in a deep formation. However, heterogeneity can significantly influenced dissolution efficiency. This work addresses the injection of CO_2 in perfectly stratified saline formations under uncertainty. Monte Carlo two-phase flow compositional simulations involving the dissolution of CO_2 into brine and evaporation of water into the CO_2-rich phase are presented. We systematically analyzed the interplay between heterogeneity and buoyant forces, which is shown to control the migration of the CO_2 plume as well as the temporal evolution of dissolution efficiency. Results show that when buoyant forces are important, vertical segregation controls the overall behavior of CO_2, diminishing the influence of small-scale heterogeneity on dissolution. However, when buoyant forces are relatively small compared to the degree of heterogeneity, CO_2 migrates preferentially through high permeability layers and dissolution efficiency increases with heterogeneity due to the stretching of the CO_2 plume that enhances mixing. As a result, in this situation, the upscaling of permeability leads to an underestimation of the dissolution efficiency. A review of field sites shows that dissolution is heterogeneity-controlled in most real systems. Knowing that most numerical models cannot afford to represent heterogeneity at an adequate scale, results indicate that dissolution efficiency can be typically underestimated by a factor close to 1.5.

1 Introduction

Geological Carbon Sequestration (GCS), which reduces carbon emissions to the atmosphere by storing the captured CO_2 in deep geologic formations, is a promising technique to mitigate climate change [*IPCC*, 2005, 2008; *Szulczewski et al.*, 2012]. Four trapping mechanisms, taking place at different time-scales, are typically distinguished to confine the CO_2 in the subsurface [*Kumar et al.*, 2005; *Riaz et al.*, 2006; *Bachu et al.*, 2007; *Vilarrasa et al.*, 2010; *Gasda et al.*, 2012]. Structural trapping, which consists of sealing the $CO_2(g)$ with a low permeable caprock, is the most rapid but unstable mechanism because $CO_2(g)$ can potentially escape the formation through faults or failed wellbore casings during seismic activities. Mineral trapping, which considers that CO_2 can dissolve in brine and react with the rock-forming minerals, is the most stable but typically slow. At intermediate time-scales, the safety of GCS is attributed to capillary trapping (residual $CO_2(g)$) and dissolution trapping (dissolved aqueous $CO_2(aq)$ in brine). These two trapping mechanisms do not directly depend on the integrity of the formation [*Van der Meer*, 1995; *Flett et al.*, 2004; *Nordbotten and Celia*, 2006; *Bryant et al.*, 2008; *Strandli and Benson*, 2013]. Capillary trapping has been well studied in the literature [*Juanes et al.*, 2006; *Ide et al.*, 2007], but fewer studies address dissolution trapping even though a substantial amount of CO_2 can potentially dissolve in the formation due to the existence of large amounts of brine solvent [e.g., *Flett et al.*, 2004; *Lee et al.*, 2010]. Numerical results reported by *Flett et al.* [2004] have shown that dissolution can trap up to 33% of the injected CO_2, which is quite close to the capillary trapping efficiency reported in the same field setting. *Lee et al.* [2010] have shown that dissolution trapping is more important than capillary trapping.

In homogeneous formations, the injected CO_2 is known to generate a smooth CO_2 plume, rising to the top of the formation by buoyant forces, and spreading laterally underneath the low permeability cap rock due to advection and dispersion; in the meanwhile, CO_2 dissolves into the brine over a long time [*Lenormand et al.*, 1988; *Bryant et al.*, 2008; *Cottin et al.*, 2010; *Green and Ennis-King*, 2010; *Mouche et al.*, 2010; *Michael et al.*, 2010; *Bandara et al.*, 2011; *Oldenburg and Rinaldi*, 2011; *Strandli and Benson*, 2013; *Plampin et al.*, 2014; *Trevisan et al.*, 2014; *Mori et al.*, 2015; *Trevisan et al.*, 2015]. However, natural formations are ubiquitously heterogeneous, affecting dissolution estimates in realistic settings. The literature in stochastic contaminant transport in saturated porous media has extensively demonstrated that heterogeneity can strongly deform solute plumes [e.g., *Zinn and Harvey*,

2003; *Knudby and Carrera*, 2005; *Fernàndez-Garcia et al.*, 2008; *Dentz et al.*, 2011; *Henri et al.*, 2015]. This deformation leads to the stretching and folding of the solute plume, which can increase the surface contact between the solute plume and the ambient groundwater. During the injection of CO_2, similar effects are expected, potentially enhancing the capacity for CO_2 dissolution. Yet, results obtained in solute transport through saturated porous media cannot be directly extrapolated to CO_2 migration during geological carbon sequestration for two major reasons: the problem involves two fluid phases controlled by viscous and gravity forces with strong nonlinear constitutive equations, and the $CO_2(g)$ plume is affected by dissolution and evaporation.

The effect of permeability stratification during the injection of $CO_2(g)$ in GCS has been observed in several works, which have demonstrated that, after injection, a major proportion of CO_2-rich phase can enter and move preferentially through relatively high permeability conduits or channels, creating erratic patterns [*Stalkup and Crane*, 1994; *McGuire et al.*, 1995; *Chadwick and Noy*, 2010a,b; *Oh et al.*, 2015; *Rasmusson et al.*, 2015; *Tsang et al.*, 2001; *Obi and Blunt*, 2006]. Data from Sleipner field site [*Gregersen*, 1998] in the North Sea, which is a reservoir formed by interbedded sandstones and mudstones, indicated that the injected $CO_2(g)$ was mostly present in several disconnected layers of relatively high permeability with a thickness of about 10 meters [*Chadwick et al.*, 2004, 2005]. This illustrates that the stratification of permeability at the meter scale (in the vertical direction) can significantly affect the fate and transport of the $CO_2(g)$ plume. Little is known about the effect that these features have on CO_2 dissolution. Although a host of literature has assessed the fate and transport of the $CO_2(g)$ plume in GCS [e.g., *Gunter et al.*, 2004; *Humez et al.*, 2011; *Kabera and Li*, 2011; *Oh et al.*, 2015], systematic high-resolution stochastic simulations of dissolution trapping in heterogeneous porous media remains lacking. The works of *Ide et al.* [2007], *Hayek et al.* [2009] and *Oh et al.* [2015] studied the effect of heterogeneity on capillary trapping, ignoring dissolution. Other authors [*Doughty et al.*, 2001; *Doughty and Pruess*, 2004; *Gershenzon et al.*, 2015a] have only analyzed dissolution trapping in a few idealized depositional settings. In numerical modeling studies, the small-scale variability of permeability is often not explicitly represented [*Birkholzer et al.*, 2009; *Hayek et al.*, 2009; *Lee et al.*, 2010; *Pruess and Nordbotten*, 2011; *Rasmusson et al.*, 2015; *Onoja et al.*, 2019]. Qualitative or quantitative analysis of the impact of discounting the small-scale variability in modeling prediction estimates of geological carbon sequestration has not been reported.

In this paper, we present high-resolution two-phase flow numerical simulations of injected $CO_2(g)$ moving though a deep saline formation during geological carbon sequestration with the objective to: (i) study the effect of heterogeneity on CO_2 dissolution; and (ii) evaluate the impact of upscaling permeability on dissolution predictions. For this, we consider one of the simplest conceptual models of heterogeneity, that is, a perfectly stratified formation system in which the permeability varies only along the vertical direction. From a practical standpoint, we note that even though perfect stratification of permeability in natural field settings is seldom observed over large horizontal distances, this model can properly represent processes over relatively short distances compared to the horizontal integral scale of permeability, which can vary from few meters to thousands of meters [e.g., *Schwartz*, 2014]. Moreover, well-connected geological formations have been shown to behave similar to a perfectly stratified system, as both exhibit continuous paths of relatively high velocity [*Zinn and Harvey*, 2003]. This type of heterogeneity has been also used in a number of investigations that explore solute transport behavior in subsurface systems [*Fernàndez-Garcia et al.*, 2008; *Mouche et al.*, 2010]. The numerical simulations we present consider a stochastic framework with multiple realizations of the permeability field, which are represented by a random space function and different degrees of heterogeneity. Dissolution efficiency is then characterized by the first two statistical moments to represent the mean behavior and its uncertainty. We show that heterogeneity and gravity forces control dissolution efficiency, and that for typical gravity forces, heterogeneity may substantially enhance dissolution efficiency. We also show that upscaling permeability can strongly compromise CO_2 dissolution predictions in highly heterogeneous systems.

The paper is organized as follows. We first present the problem and the mathematical description in Sections 2 and 3, respectively. We then introduce the computational approach adopted during simulations in Section 4. After this, in Section 5, we present the results. Section 5.1 shows how buoyant forces and heterogeneity affect CO_2 dissolution efficiency, and Section 5.2 illustrates how upscaling the permeability impacts on CO_2 dissolution efficiency. Finally, conclusions are summarized in Section 6.

2 Problem Statement

We consider the injection of supercritical CO_2 through a fully-penetrating well in a deep confined saline formation. The formation is conceptualized as a perfectly stratified formation. Heterogeneity is represented by the spatial variability of the intrinsic permeability, which is assumed to vary in space only as a function of the z-coordinate. We consider the existence of two immiscible fluid phases, the brine phase (l) and the CO_2-rich phase (g), which are separated by a distinct interface, characterized by a spatially varying retention curve. Brine is represented by a high-concentration solution of Sodium Chloride ($NaCl$) in water (H_2O). Initially, the formation is considered to be fully saturated with brine. Once injected, the CO_2 enters into the formation, displacing the brine and rising towards the top of the formation by bouyant forces. During the migration of CO_2, dissolution of CO_2 into brine and evaporation of water into the CO_2-rich phase takes place. The time scale for dissolution and evaporation is smaller than the time scale for transport, and therefore, we consider that reactions are always in local equilibrium [*Xu et al.*, 2004, 2011; *Leal et al.*, 2013]. Other reactions are not considered and the temperature is assumed constant. For brevity, the injected supercritical CO_2 is called gas.

3 Mathematical Description

3.1 Chemical System

The chemical system is composed of three chemical components $\{CO_2, H_2O, NaCl\}$. The first two chemical components $\{CO_2, H_2O\}$ can exist in both liquid and gas phases according to the equilibrium constants of dissolution and evaporation. Thus, mutual solubility between brine and CO_2-rich phases is taken into account. $NaCl$ remains only in the brine phase. The changes in salinity due to dissolution/evaporation is assumed to be negligible and thereby the molality of $NaCl$ is assumed constant. In total, we have five chemical species: $CO_2(g)$, $CO_2(aq)$, $H_2O(g)$, $H_2O(l)$ and $NaCl(aq)$. The partition of the chemical species between phases is determined by the following equilibrium chemical reactions,

$$H_2O(l) \Leftrightarrow H_2O(g), \qquad K^H = f_g^H / a_l^H, \tag{1}$$

$$CO_2(aq) \Leftrightarrow CO_2(g), \qquad K^C = f_g^C / a_l^C, \tag{2}$$

where the subscripts l, g and aq denote the liquid, the gas and the aqueous state, respectively, and the superscript C and H denote the CO_2 and H_2O components, respectively. K^H and K^C are the equilibrium constants, and f_g^β and a_l^β respectively denote the fugacity and the activity of the β chemical component. We follow the partitioning model for CO_2-brine mixtures presented by *Spycher and Pruess* [2005] to estimate mass compositions in liquid and gas phases.

3.2 Mass Balance equations

The migration of CO_2 in the saline formation is simulated using a compositional approach. Given that the salinity is constant, we only need two mass balance equations. The

macroscopic mass balance equations for the two chemical components of interest $\{CO_2, H_2O\}$ can be written as

$$0 = \mathcal{F}_1 = \sum_{\alpha=l,g} \left[\frac{\partial(\phi S_\alpha \rho_\alpha X_\alpha^H)}{\partial t} + \nabla \cdot (\rho_\alpha X_\alpha^H \boldsymbol{q}_\alpha) - \nabla \cdot (\phi S_\alpha \boldsymbol{D}_\alpha \rho_\alpha \nabla X_\alpha^H) \right] - Q_g^H, \tag{3}$$

$$0 = \mathcal{F}_2 = \sum_{\alpha=l,g} \left[\frac{\partial(\phi S_\alpha \rho_\alpha X_\alpha^C)}{\partial t} + \nabla \cdot (\rho_\alpha X_\alpha^C \boldsymbol{q}_\alpha) - \nabla \cdot (\phi S_\alpha \boldsymbol{D}_\alpha \rho_\alpha \nabla X_\alpha^C) \right] - Q_g^C, \tag{4}$$

where ϕ [-] is the formation porosity, S_α [-] is the saturation of the α-phase, ρ_α [kg·m^{-3}] is the density of the α-phase, X_α^β [-] represents the mass fraction of component β in phase α, $\boldsymbol{D}$ [m^2· s^{-1}] is the hydrodynamic dispersion tensor, Q_g^H and Q_g^C [kg· s^{-1}] are the source terms, and $\boldsymbol{q}_\alpha$ is the fluid flux associated with the α phase given by Darcy's law,

$$\boldsymbol{q}_\alpha = -\frac{\kappa \kappa_{r\alpha}}{\mu_\alpha} (\nabla p_\alpha + \rho_\alpha g \nabla z), \tag{5}$$

where κ [m^2] is the intrinsic permeability, $\kappa_{r\alpha}$ [-] is the relative permeability of phase α, μ_α [pa· s] is the viscosity, p_α [pa] is the fluid pressure, and g [m· s^{-2}] is the gravitational acceleration. Mass balance equations are subject to the following constraints,

$$\omega X_l^H + X_l^C = 1, \tag{6}$$

$$X_g^H + X_g^C = 1, \tag{7}$$

$$S_l + S_g = 1, \tag{8}$$

where $\omega = 1 + 0.05844 m_l^S$. Here, we have assumed that the salt only comprises $NaCl$, and the molality of $NaCl$ (m_l^S) is fixed.

3.3 Constitutive Equations

The saturation of the liquid phase is assumed to be known from the capillary pressure through the $CO_2 - H_2O$ retention curve. In this work, we used the *van Genuchten* [1980] model for the retention curve, which determines that

$$S_{le}(p_c) = \begin{cases} 1, & p_c < 0 \\ [1 + (\sqrt{\frac{\kappa}{\kappa_g}} \alpha_p p_c)^{n_p}]^{-m_p}, & p_c \geq 0, \end{cases} \tag{9}$$

where p_c is the capillary pressure between the two immiscible fluids, defined as $p_c = p_g - p_l$, κ_g [m^2] is the geometric mean of the intrinsic permeability, $m_p = 1 - 1/n_p$, α_p [bar^{-1}] is the scaling parameter of the retention curve, and S_{le} is the effective liquid saturation, defined as

$$S_{le} = \begin{cases} 1, & S_l > 1 - S_{gr} \\ \frac{S_l - S_{lr}}{1 - S_{lr} - S_{gr}}, & S_{lr} \leq S_l \leq 1 - S_{gr} \\ 0, & S_l < S_{lr}, \end{cases} \tag{10}$$

where S_{lr} [-] and S_{gr} [-] are the residual saturations of brine and CO_2-rich phases, respectively. The Leverett J-function has been used to describe the relationship between the entry

pressure and the permeability of the porous medium [*Juanes et al.*, 2006; *Plug and Bruining*, 2007; *Krevor et al.*, 2011, 2015]. The porosity is assumed constant. The relative permeabilities for the two phases are respectively given as

$$\kappa_{rl} = \kappa_{rlm} \cdot (S_{le})^{\epsilon_p} [1 - (1 - S_{le}^{1/m_p})^{m_p}]^2, \tag{11}$$

$$\kappa_{rg} = \kappa_{rgm} \cdot (1 - S_{le})^{\gamma_p} (1 - S_{le}^{1/m_p})^{2m_p}, \tag{12}$$

where κ_{rlm}, κ_{rgm}, ϵ_p and γ_p are the scaling parameters. Hysteresis of the retention curve and the relative permeability curve is not considered. The dispersion tensor is given as

$$\boldsymbol{D}_\alpha = D_m \boldsymbol{I} + \alpha_L |\boldsymbol{v}_\alpha| + (\alpha_L - \alpha_T) \frac{\boldsymbol{v}_\alpha \boldsymbol{v}_\alpha^t}{|\boldsymbol{v}_\alpha|}, \tag{13}$$

where $\boldsymbol{I}$ is identity matrix, D_m is molecular diffusion coefficient, α_L and α_T are respectively the longitudinal and transverse dispersivities, and $\boldsymbol{v}_\alpha = \boldsymbol{q}_\alpha/(\phi S_\alpha)$ [*Saaltink et al.*, 2013]. The density and viscosity of the two fluids is affected by the fluid pressures and their mass compositions according to *Garcia* [2003] and *Wang* [2022].

3.4 Numerical Solution

We developed a MATLAB-based fully-coupled integrated finite difference code to solve the system of transport equations given by (3) and (4) using a fully implicit method based on the Newton-Raphson algorithm. Details can be found in Appendix C. The liquid brine pressure p_l and the CO_2-rich phase pressure p_g are selected as independent variables. The rest of variables can be explicitly expressed as functions of p_l and p_g through the constitutive equations and the equations of state. This selection of independent variables is convenient in dealing with phase appearance and disappearance [*Bourgeat et al.*, 2010; *Angelini et al.*, 2011; *Ern and Mozolevski*, 2012; *Neumann et al.*, 2013; *Saaltink et al.*, 2013]. The time step is chosen to satisfy the Courant–Friedrichs–Lewy (CFL) condition, i.e., for any grid cell of the domain and flow direction we impose that,

$$\frac{q\mathcal{S}\Delta t}{\phi V_c} = \mathrm{Cu}, \quad q = \max(q_l, q_g), \tag{14}$$

where q is the maximum flux of the two phases, Cu is the courant number fixed to 0.2, $\mathcal{S}$ is the cross-sectional area transverse to the flux, V_c is the grid cell volume, and Δt the time step. The time step is very sensitive to phase appearance and disappearance. When the simulation experiences phase appearance/disappearance at a given point, Δt is automatically reduced to a very small value (e.g., 0.1 second), and then gradually increased following a geometric progression with a common ratio of 3 until the CFL condition is again satisfied. The code is capable to simulate injection wells penetrating through different layers. For this, the mass flux that is transferred to the nth node of the well is given by the pressure difference between the node and the well as,

$$Q_{g,n}^C = X_g^C \rho_g \frac{2\pi\kappa_n b_n}{\ln(r_e/r_w)} \frac{\kappa_{rg}}{\mu_g} \left(p_{wg,n} - p_{g,n}\right), \tag{15}$$

$$Q_{g,n}^H = X_g^H \rho_g \frac{2\pi\kappa_n b_n}{\ln(r_e/r_w)} \frac{\kappa_{rg}}{\mu_g} \left(p_{wg,n} - p_{g,n}\right). \tag{16}$$

where b_n is the saturated thickness of the cell, r_w and r_e are respectively the well radius and effective well radius, and $p_{g,n}$ and $p_{wg,n}$ are the gas phase pressure and well pressure

at node n, respectively. The well pressure is calculated based on the bottom hole pressure (p_{bh}) at reference location (z_{bh}) through $p_{wg,n} = p_{bh} + \rho_g g(z_{bh} - z_n)$. Mass balance at the injection well is written as,

$$Q_{well} = \sum_{n \in N_{well}} Q^C_{g,n} + Q^H_{g,n}, \tag{17}$$

where Q_{well} is the total mass injection rate of the CO_2 gas phase, and N_{well} is the number of grid-cells pierced by the injection well.

4 Computational Approach

4.1 Model Setup

We consider a confined saline formation with an isolated fully-penetrating well centered in the middle. The system is represented by an axisymmetric model defined by cylindrical coordinates (r,φ,z). The z-axis coincides with the center of the fully-penetrating well. Figure 1 shows a sketch diagram of the model setup. By symmetry, the solution does not depend on the angular coordinate φ. The top and bottom boundaries are impermeable boundaries, and the outer boundary has constant liquid pressure and zero saturation gradient. The system is initially saturated with brine, which is assumed to be at hydrostatic state, i.e., the liquid pressure increases downward with a vertical gradient given by the specific gravity of the liquid phase, $\rho_l g$. The injected $CO_2(g)$ is saturated with water vapor. This is mostly the case in real applications because dry CO_2 can trigger the dissolution of minerals, such as halite, and reduce well injectivity. The radius of the injection well is 0.1 [m]. The initial liquid pressure is $p_{li} = 150$ [bar] on the top layer, and the initial gas pressure is $p_{gi} = 1$ [bar] everywhere. CO_2 is injected at a constant mass injection rate Q_{well}. The parameters adopted during the simulations are summarized in Table 1. With these parameters, $Q_{well} \approx Q^C_g$ and Q^H_g is very small ($\sim$ 0.2‰). The simulation is terminated when the total injected mass of CO_2 reaches a value of $M_{inj} = 2.5$ [Mt]. The concentration of $NaCl$ (m^S_l) is fixed to 0.5 [molal] and the temperature (T_c) is 60 [°C]. The axisymmetric model grid discretization consists of N_z layers and N_r coaxial rings around the z-axis. The discretization is uniform in the vertical direction but increases linearly with r.

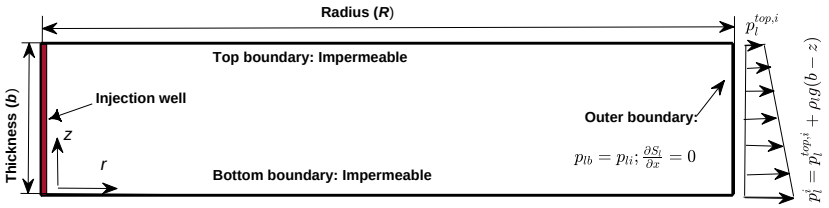

Figure 1: Sketch of the simulation setup.

4.2 Model Validation

The numerical code is tested against the semi-analytical solution developed by *Nordbotten and Celia* [2006], which provides the vertical location of the interface between the gaseous CO_2 and the brine phases. The model setup is also represented by Figure 1. However, in order to satisfy the analytical solution requirements, the permeability, fluid densities, and fluid viscosities are assumed constant, and the relative permeability is assumed to be linearly proportional to saturation. Table 2 provides a summary of the parameters adopted for

Table 1: Summary of the parameters adopted during Monte Carlo simulations.

Parameters	**Symbol**	**Units**	**Values**
Domain size	(R, b)	[m]	(5000, 100)
Grid discretization	(N_r, N_z)	[-]	(100, 100)
Porosity	ϕ	[-]	0.1
Initial liquid pressure	p_{li}	[bar]	150
Initial gas pressure	p_{gi}	[bar]	1
Well radius	r_w	[m]	0.1
Total injection mass	M_{inj}	[Mt]	2.5
Parameter for Eq. (9)	α_p	[bar^{-1}]	5
Parameter for Eq. (9)	m_p	[-]	0.8
Parameters for Eqs. (11)-(12)	$(\kappa_{rlm}, \kappa_{rgm})$	[-]	(1,1)
Parameters for Eqs. (11)-(12)	(ϵ_p, γ_p)	[-]	(0.5,0.5)
Residual saturations	(S_{lr}, S_{gr})	[-]	(0.2,0)
Hydrodynamic dispersivities	(α_L, α_T)	[m]	(5,1)
Molecular diffusion coefficient	D_m	[m^2·s^{-1}]	10^{-9}
Salinity	m_l^S	[molal]	0.5
Temperature	T_c	[°C]	60

model validation. The table only shows the parameters that have changed from the model setup listed in Table 1. For comparison purposes, we estimated the location of the interface by balancing the area of the saturation distribution above and below the interface to preserve mass balance,

$$z(r) = b - \int_0^b S_g(r, z)dz. \tag{18}$$

The comparison between the analytical and numerical solution is shown in Figure 2, from which we can see that, the numerical result agree well with the theoretical solution. The size of the $CO_2(g)$ plume given by the numerical solution is slightly smaller than the analytical solution because the numerical simulation still considers the dissolution of CO_2 into brine.

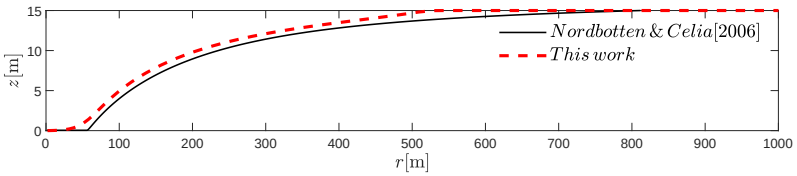

Figure 2: Comparison of the numerical result with the theoretical solution by *Nordbotten and Celia* [2006].

Table 2: Parameter settings adopted for the model validation.

Parameters	**Symbol**	**Units**	**Values**
Domain size	(R, b)	[m×m]	(2000,15)
Grid discretization	(N_r, N_z)	[-]	(100,20)
Intrinsic permeability	κ	[m^2]	2×10^{-14}
Porosity	ϕ	[-]	0.15
Initial pressures	$\left(p_l^{top,i}, p_g^i\right)$	[bar]	(150,10)
Well radius	r_w	[m]	0.1
Injection rate	Q_{well}	[Mt/year]	0.028
Simulation time	T_s	[day]	5194
Viscosities	(μ_l, μ_g)	[mpa·s]	(0.511,0.061)
Densities	(ρ_l, ρ_g)	[kg·m^{-3}]	(1099,733)

4.3 Performance Metric

The analysis of the simulation results is based on the quantification of the total amount of CO_2 dissolved into brine with respect to the total amount of CO_2 injected per unit of time. We therefore define the following performance metric for measuring dissolution efficiency,

$$E(t) = \frac{\mathcal{M}_d(t+\Delta t) - \mathcal{M}_d(t)}{\mathcal{M}_{inj}(t+\Delta t) - \mathcal{M}_{inj}(t)}, \tag{19}$$

where $\mathcal{M}_{inj}(t)$ is the total injected mass of CO_2 at time t, $\mathcal{M}_d(t)$ is the total dissolved mass of CO_2 at time t, and Δt is the time step. Numerically, the mass of dissolved CO_2 into brine is indirectly calculated from the mass of undissolved CO_2 as

$$E(t) = \frac{Q_g^C \Delta t - \sum_i [X_g^C S_g \phi V_c \rho_g]_i^{t+\Delta t} + \sum_i [X_g^C S_g \phi V_c \rho_g]_i^t}{Q_g^C \Delta t}, \tag{20}$$

where V_c is grid cell volume, i denotes the ith grid cells, and Q_g^C is the mass injection rate of CO_2.

4.4 Stochastic Framework

The simulation approach considers a stochastic description of the natural log of the intrinsic permeability $Y(\mathbf{x}) = \ln \kappa(\mathbf{x})$. The $Y(\mathbf{x})$ random field follows a correlated random space function, characterized by an anisotropic exponential covariance function with mean $\overline{Y}$, variance σ_Y^2, vertical correlation length I_v, and a very large horizontal integral scale I_h. We consider that I_h is much larger than the domain size and therefore, for practical purposes, $I_h \to \infty$. The geometric mean of the permeability is $\kappa_g = 1\cdot10^{-13}$ [m^2]. The integral scale in the vertical direction l_v is fixed to 5 [m]. We used three different variances σ_Y^2 and six different mass injection rates Q_{well} to analyze the effect of heterogeneity and buoyant forces under different degrees of heterogeneity. Buoyant forces are characterized by the gravity factor G, which is defined as the ratio of gravity forces resulting from fluid density differences to the viscous forces [*Nordbotten and Celia*, 2006], that is,

$$G = \frac{2\pi\Delta\rho\rho_g g \kappa_h b^2}{Q_{well}\mu_l}, \tag{21}$$

where $\Delta\rho = \rho_l - \rho_g$, b is the thickness of the formation, and k_h is the effective vertical permeability, which is the harmonic mean in this case. The density of the fluids and the viscosity slightly change with time during the simulations. Based on this, to estimate the gravity factor, we chose to use the spatial mean of these properties obtained at the end of the injection. Synthetic test cases are summarized in Table 3. Larger values of G indicate larger density differences between the two fluids and therefore a higher potential for vertical segregation of CO_2.

Random fields are simulated with the following procedure. We first generate 50 equally likely realizations of a standardized multiGaussian random field $Y_{std}(\mathbf{x})$, characterized by a zero mean and unit variance, with the Sequential Gaussian Simulation method implemented in the SGSIM code [*Journel and Huijbregts*, 1976]. For each test case, these 50 standardized realizations are rescaled by $Y(\mathbf{x}) = \overline{Y} + \sigma_Y Y_{std}(\mathbf{x})$ to satisfy the target statistical properties. We then simulate the injection of CO_2 in each realization. The dissolution trapping efficiency $E(t)$ is then characterized by their statistical moments (mean behavior and coefficient of variation). A review of typical statistical properties, mass injection rates and inherent gravity forces from real GCS field applications is shown in Table 4. The parameters adopted in our simulations in terms of mass injection rates and gravity forces are representative of real field applications.

Table 3: Statistical properties of the random fields and mass injection rates in the different simulated cases.

Case	$\boldsymbol{Q_{well}}$ [Mt/y]	$\boldsymbol{\kappa_g}$ [m^2]	$\boldsymbol{\sigma_Y^2}$ [-]	$\boldsymbol{I_v}$ [m]	$\boldsymbol{\langle G \rangle}$ [-]
1	6.92	10^{-13}	0.1	5.0	0.13
2	2.50	10^{-13}	1.0	5.0	0.13
3	1.80	10^{-13}	4.0	5.0	0.13
4	0.69	10^{-13}	0.1	5.0	1.3
5	0.25	10^{-13}	1.0	5.0	1.3
6	0.18	10^{-13}	4.0	5.0	1.3

4.5 Upscaling of Permeability

Since the scale of heterogeneity is typically smaller than the size of the numerical discretization used in most groundwater models, numerous authors have investigated whether one can simplify the flow system by substituting the heterogeneous distribution of κ by a representative value. Results in this matter are well established in the literature and reviewed in several papers and books [e.g., *Wen and Gómez-Hernández*, 1996; *Renard and de Marsily*, 1997; *Sanchez-Vila et al.*, 2006]. In particular, it is well-known that the equivalent permeability of a perfectly stratified medium is the arithmetic mean κ_a of the point permeabilities when the flow is parallel to the stratification and the harmonic mean κ_h when the flow is perpendicular to the strata. In our system, that is to say that the equivalent permeability is a second-order symmetric tensor exactly given by

$$\mathbf{K}^e = \begin{bmatrix} \kappa_a & 0 \\ 0 & \kappa_h \end{bmatrix}. \tag{22}$$

In this context, this work also evaluates the effect of upscaling permeability on CO_2 dissolution. To achieve this, for each realization of the $Y(\mathbf{x})$ field and test case, we also simulate the injection of CO_2 assuming that the system is homogeneous and characterized by an

Table 4: Review of formation statistical properties, mass injection rates and gravity forces from real geological carbon sequestration field sites.

Reservoir	Changhua Coastal Industrial Park[1]	Buzzard's Bench[2]	Ordos Basin[3]	Sleipner[4]	Tubåen[5]	In Salah[6]
Location	Taiwan	US	China	Norway	Norway	Algeria
Depth [m]	~2220	~2025	~1845	~950	~2470	~1860
Thickness [m]	~1000	~150	~290	~300	~60	~20
κ_g [m^2]	9.8×10^{-15}	2.6×10^{-14}	2.7×10^{-16}	1×10^{-12}	5×10^{-13}	1×10^{-14}
σ_Y^2[-]	6.9^a	5.5^b	2.9^a	10.6^a	5.5^b	-
ϕ [-]	0.16	0.16	0.11	0.35	0.13	0.15
m_l^S[molal]	0.5	0.3	0.3	0.6	2.4	-
Q_{well}[Mt/year]	1.0	1.87	0.1	0.84	0.77	1.0
G[-]	0.07	0.03	0.04	$< 10^{-3}$	1.12	0.002

Reference: [1]*Sung et al.* [2014],[2]*Xiao et al.* [2019],[3]*Wang et al.* [2016], *Jing et al.* [2019], [4]*Arts et al.* [2008] and *Michael et al.* [2010], [5]*Maldal and Tappel* [2004] and *Grude et al.* [2013], and [6]*Mathieson et al.* [2009, 2011].
^{a} calculated from log data. ^{b} calculated from $\sigma_Y^2 \approx R^2/3$, where $R = \log(\kappa_{max}/\kappa_{min})$, as given by *Fogg and Zhang* [2016].

equivalent anisotropic permeability tensor given by $\mathbf{K}^e$. The rest of the parameters are kept the same.

5 Results

To facilitate the interpretation, results are presented using dimensionless variables, defined according to *Nordbotten and Celia* [2006], *Silin et al.* [2009] and *Zhao et al.* [2014] as

$$t^* = \frac{t}{t_c}, \quad \zeta = \frac{z}{b}, \quad \xi = \frac{r}{\ell}, \quad S_{ge} = \frac{S_g - S_{gr}}{1 - S_{lr} - S_{gr}}, \tag{23}$$

where b is the thickness of the geological formation, S_{ge} is the effective gas saturation, and t_c and ℓ are the characteristic time and length scales, respectively defined as

$$t_c = \frac{\phi\mu_l b}{\Delta\rho g \kappa_g}, \quad \ell^2 = \frac{M_{inj}}{2\pi\phi\rho_g b}. \tag{24}$$

In accordance with *Zhao et al.* [2014], t_c is an approximate estimate of the time needed for the CO_2 to migrate from the bottom of the formation to the top due to buoyant forces. ℓ is a measure of the radial penetration of CO_2 due to advection only.

5.1 Effect of Heterogeneity and Buoyant Forces

In this section, we present the effect of heterogeneity and buoyant forces, and their interplay, on CO_2 dissolution. Figures 3 and 4 show the temporal evolution of the ensemble average of dissolution efficiency and its uncertainty (expressed by the coefficient of variation) for a relatively small and large gravity factor, respectively. In all cases, the temporal evolution exhibits two clear dissolution regimes, characterized by the characteristic time of gravity segregation t_c. At early times ($t < t_c$), gravity segregation controls CO_2 migration, and dissolution efficiency strongly declines with time. After this, for $t > t_c$, when grav-

ity segregation has already developed, the less dense $CO_2(g)$ is overriding the brine, and $CO_2(g)$ plume is mostly spreading laterally. At this point, dissolution efficiency reaches a quasi steady-state behavior with a clear asymptotic value. The decline of dissolution efficiency is attributed to the following. At the very beginning, all the injected CO_2 dissolves into the brine (dissolution efficiency is 100%) until brine becomes saturated and the gas phase appears. After this, the rising of $CO_2(g)$ due to buoyant forces enhances the contact between the brine and gas phases, favoring the mixing between them and therefore dissolution. This process decays with the segregation of $CO_2(g)$ at the top of the formation. After this, $CO_2(g)$ is forced to move laterally by viscous forces, which leads to a steady growth of the interface and thus dissolution efficiency.

Results show that dissolution efficiency generally increases with σ_Y^2. This effect is more pronounced when the gravity factor is relatively small ($\langle G \rangle$=0.13). In order to visually understand this effect, in the left panels of Figures 5 and 6, we present the spatial distribution of $CO_2(g)$ saturation obtained at the end of the injection in a representative realization of the permeability field for different σ_Y^2 and mean gravity factors. Note that, by construction, the underlying heterogeneous structure of the permeability field is the same. Results corroborate the hypothesis that heterogeneity tends to stretch the interface between the gas and liquid phases through preferential channels, increasing the contact between them, and therefore, effectively increasing the mutual solubility between the two phases.

Importantly, results also show that heterogeneity and buoyant forces constitute two important competing factors that control dissolution efficiency. When buoyant forces are relatively low compared to the degree of heterogeneity ($G < \sigma_Y^2$), heterogeneity is the dominant factor and CO_2 migration mostly takes place laterally through high permeability layers, regardless of the buoyant forces. In contrast, when the gravity factor is relatively large compared to the degree of heterogeneity ($G > \sigma_Y^2$), gravity segregation is the dominant process. In this case, vertical segregation is overwhelming and the CO_2 gas plume floats to the top of the formation regardless of the permeability stratification. These features can also be seen in Figures 5 and 6 by contrasting, for instance, the results obtained with $\langle G \rangle$=0.13 against those with $\langle G \rangle$=1.3 for $\sigma_Y^2 = 1$. In this case, the CO_2 gas plume tends to segregate on top of the formation for $\langle G \rangle$=1.3, while preferentially moving through a high permeability layer when $\langle G \rangle$=0.13. In all cases, when $\sigma_Y^2 = 4$, the CO_2 gas plume preferentially concentrates in the most permeable layer.

Our simulated dissolution efficiency values are consistent with those reported in the literature. When $\langle G \rangle = 1.3$ and $\sigma_Y^2 = 1$, we obtain that the dissolution efficiency is around 20%, which is similar to those reported by *Li et al.* [2017] and *Li et al.* [2018] for a synthetic test case with $G \approx 10^3$ and $\sigma_Y^2 = 1.5$. *Al-Khdheeawi et al.* [2017] also reported an average solubility trapping of approximately 20% in several synthetic homogeneous aquifers with $G \approx 68$. Numerical simulations of the Changhua Coastal Industrial Park field site [*Sung et al.*, 2014] reported a dissolution efficiency of 15.6%. Smaller values are also reported in the literature. *Zhou et al.* [2008] and *Zhou et al.* [2010] obtained that approximately 7% of the injected CO_2 dissolves into brine when the gravity factor ranges between 0.7 and 2.2. We attribute this to the high brine salinity used (around 4 [molal]), which reduces the mass fraction of $CO_2(aq)$ in brine to only around 2.5%. Finally, we notice that in agreement with our results, *Zhang et al.* [2017] also concluded that the dissolution efficiency was insensitive to heterogeneity for $G \approx$19 and σ_Y^2 smaller than 4.5.

The uncertainty associated with dissolution efficiency is shown in the bottom panels of Figures 3 and 4. The temporal evolution of CV_E also exhibits two differentiated regimes characterized by t_c. In general, CV_E increases with time as the dissolution efficiency decreases. At large times, when $t > t_c$, CV_E approaches a relatively constant value. As expected, CV_E is larger when dissolution is controlled by the heterogeneity, i.e., when $\sigma_Y^2 > G$. In this case, we can see that the uncertainty increases with σ_Y^2. When the process is controlled by the gravity segregation, i.e., $G > \sigma_Y^2$, the uncertainty due to σ_Y^2 is reduced. The reason is that when the system is controlled by buoyant forces, the CO_2 tends to float and

segregate on the top of the formation, following more or less the same pattern regardless of the distribution of permeability. As a result, the variability in permeability is not strongly transferred to the spatial distribution of CO_2. This is clearly seen in Figure 6, which shows that the distribution of gas saturation for $\sigma_Y^2 = 0.1$ and $\sigma_Y^2 = 1.0$ still shared very similar features.

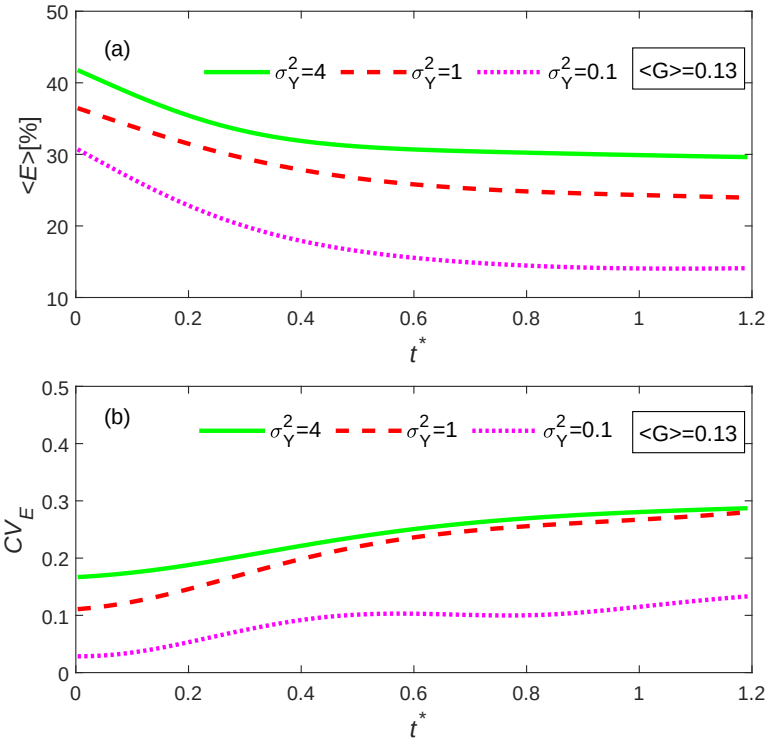

Figure 3: (a) Temporal evolution of the ensemble average dissolution efficiency <E> as a function of the degree of heterogeneity for a mean gravity factor of 0.13 (normal injection rate); (b) Temporal evolution of the corresponding coefficient of variation of the dissolution efficiency.

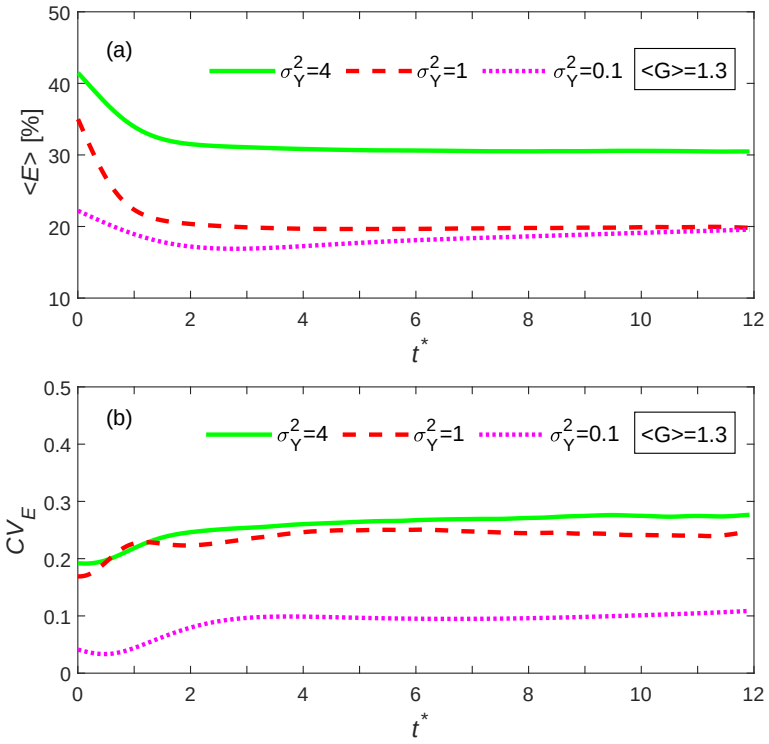

Figure 4: (a) Temporal evolution of the ensemble average dissolution efficiency <E> as a function of the degree of heterogeneity for a mean gravity factor of 1.3 (relatively slow injection rate); (b) Temporal evolution of the corresponding coefficient of variation of the dissolution efficiency.

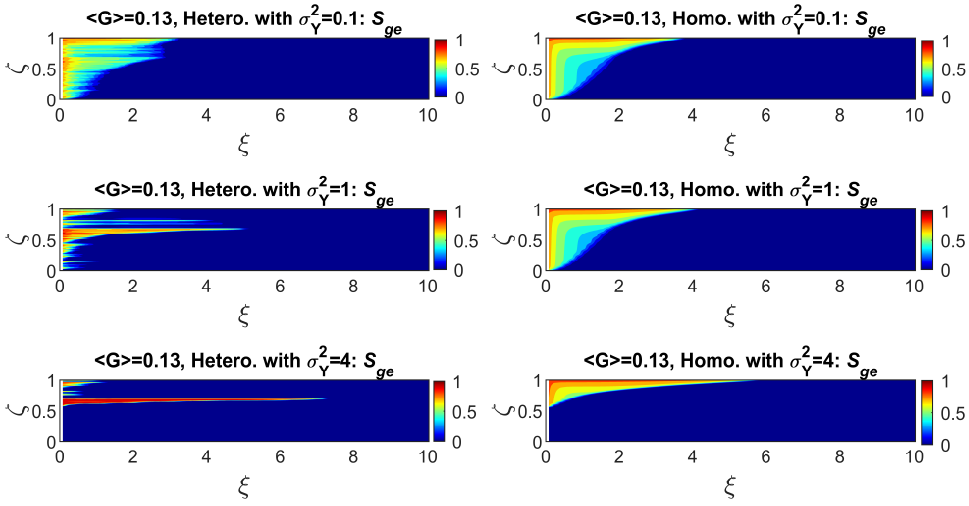

Figure 5: Spatial distribution of $CO_2(g)$ saturation obtained with a large gravity factor at the end of the injection (t=1.2t_c): (left column) in a representative heterogeneous realization with different rescaled σ_Y^2; and (right column) in the corresponding equivalent homogeneous medium.

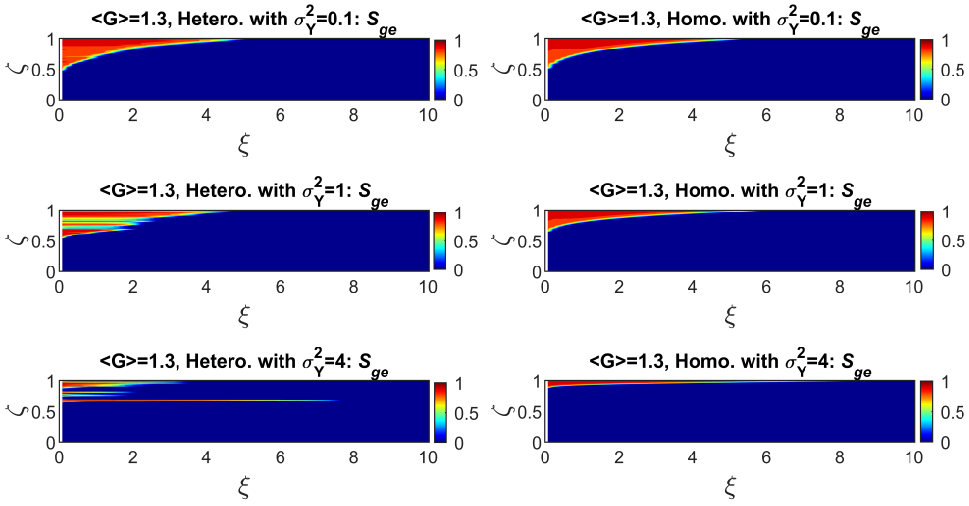

Figure 6: Spatial distribution of $CO_2(g)$ saturation obtained with a small gravity factor at the end of the injection (t=12t_c): (left column) in a representative heterogeneous realization with different rescaled σ_Y^2; and (right column) in the corresponding equivalent homogeneous medium.

5.2 Impact of Upscaling the Permeability

In this section, we present the impact that upscaling the permeability has on dissolution efficiency. To achieve this, for each realization, we substitute the heterogeneous distribution of permeability by an equivalent homogeneous porous medium, characterized by an anisotropic permeability tensor defined by equation (22). The dissolution efficiency obtained in the equivalent homogeneous medium is denoted as E_0. The loss of dissolution efficiency during the upscaling process is expressed by the reduction factor E/E_0. Figures 7 and 8 show the temporal evolution of the ensemble average of E/E_0 as a function of σ_Y^2 for the two different gravity factors. Results indicate that upscaling can lead to a significant underestimation of dissolution efficiency in heterogeneity-controlled problems, i.e., $G < \sigma_Y^2$. In these cases, the homogenization of the permeability field does not properly preserve the interplay between the small-scale spatial variability of permeability and dissolution, which is characterized by abrupt changes in permeability that enhance the contact between the gas and brine phases. This is emphasized by the nonlinear nature of the CO_2-Brine system; the less viscous $CO_2(g)$ preferentially enters into high permeable layers, increasing the mobility of $CO_2(g)$ and thus further enhancing the $CO_2(g)$ flux [*Rasmusson et al.*, 2015]. This nonuniform displacement is also partially attributed to the low capillary entry pressure in the high permeable layers. For $G = 0.13$ and $\sigma_Y^2 = 4$, we found that dissolution efficiency is reduced by a factor close to 1.5 due to upscaling. This reduction factor increases with σ_Y^2 and decreases with G. When $G > \sigma_Y^2$, the problem is gravity-controlled and the upscaling of permeability does not introduce an obvious discrepancy in the estimation of the dissolution efficiency.

In order to visually understand the effect of upscaling on dissolution, Figures 5 and 6 compare the spatial distribution of CO_2 gas saturation obtained in heterogeneous field (left panels) with their corresponding equivalent homogeneous simulations (right panels). Support information provides additional data on mass fractions. When $G > \sigma_Y^2$, the effect of gravity segregation controls CO_2 plume migration and the injected $CO_2(g)$ floats to the top of the formation regardless of stratification. In this case, buoyant forces destroy the action of heterogeneity, causing an apparent homogenization of the porous media. As a result, the simulated CO_2 plumes obtained in heterogeneous porous media resembles those of the equivalent homogeneous porous medium. This explains why the reduction factor E/E_0 is close to 1 in this case. When $G < \sigma_Y^2$, gravity segregation is overwhelmed by the stratification of permeability. In this case, the injected CO_2 mostly enters into high-permeable layers and dissolves therein, and the $CO_2(g)$ plume distribution departs from the equivalent homogeneous medium. In this case, the CO_2 plume fringe looks erratic with CO_2 preferentially flowing through several highly conductive layers without apparently floating to the top of the formation. Therefore, small-scale inclusions of high permeable layers fundamentally control the shape, dynamics and hence the dissolution of CO_2 [*Gershenzon et al.*, 2015b,c,a]. In this case, the reduction factor of dissolution efficiency increases with σ_Y^2.

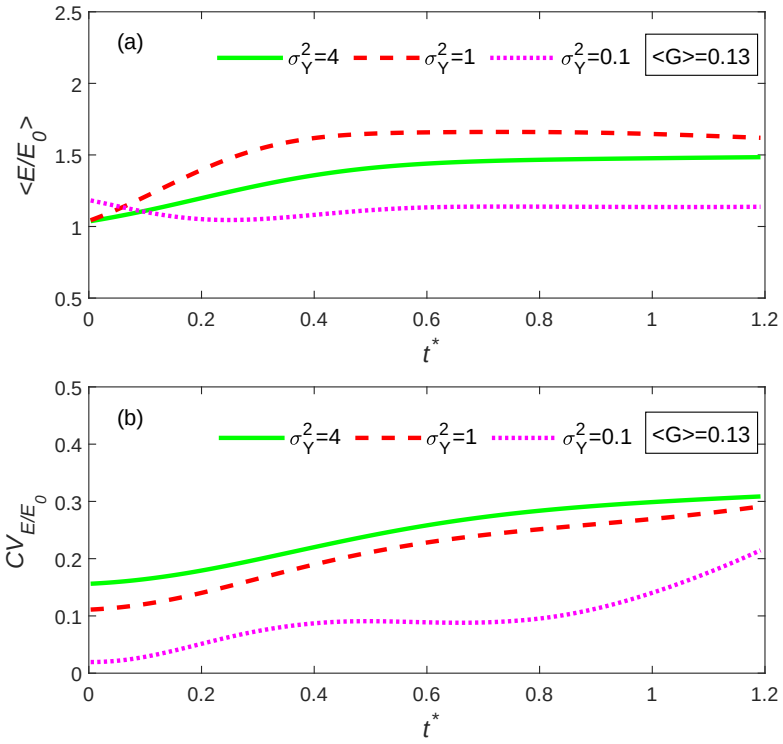

Figure 7: (a) Temporal evolution of the reduction factor $\langle E/E_0 \rangle$ in dissolution efficiency for a mean gravity factor of 0.13 due to the upscaling of permeability; (b) Temporal evolution of the corresponding coefficient of variation of the reduction factor in dissolution efficiency.

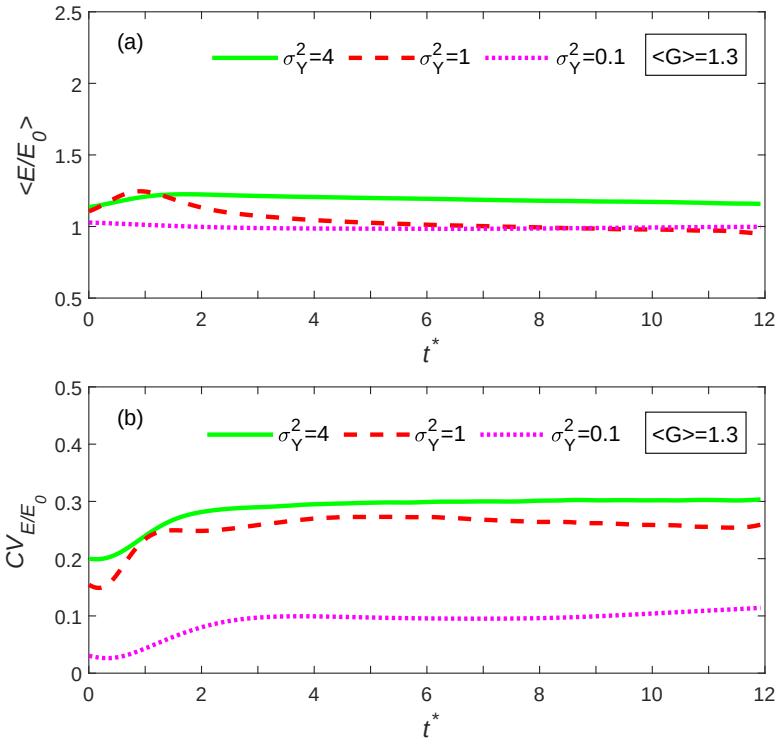

Figure 8: (a) Temporal evolution of the reduction factor $\langle E/E_0 \rangle$ in dissolution efficiency for a mean gravity factor of 1.3 due to the upscaling of permeability; (b) Temporal evolution of the corresponding coefficient of variation of the reduction factor in dissolution efficiency.

5.3 Implications

From a practical point of view, our results indicate that dissolution efficiency can be quite important in complex heterogeneous systems when $G \ll \sigma_Y^2$. Under these conditions, we find that dissolution efficiency can reach values over 30%. At this stage, it is important to highlight that, in most geological formations, the permeability varies in space over 3 orders of magnitude, which means that σ_Y^2 can easily exceed a value of 3 [*Fogg and Zhang*, 2016]. Consequently, the enhancement of dissolution efficiency observed in our simulations due to small-scale heterogeneity might be the rule rather than the exception in real field settings. To illustrate this, we map the properties associated with the GCS field sites reviewed in Table 4 in a behavior diagram, shown in Figure 9. The $\sigma_Y^2 - G$ diagram has been qualitatively drawn from a limited number of simulations and therefore uncertainties associated with transition lines are expected. Nevertheless, the diagram clearly shows that most field sites are heterogeneity-controlled, meaning that dissolution efficiency might be larger than expected. This is consistent with *Goodman et al.* [2013] and *Gershenzon et al.* [2015a], who suggest that incorporating the small-scale heterogeneity is critical to reproduce GCS processes.

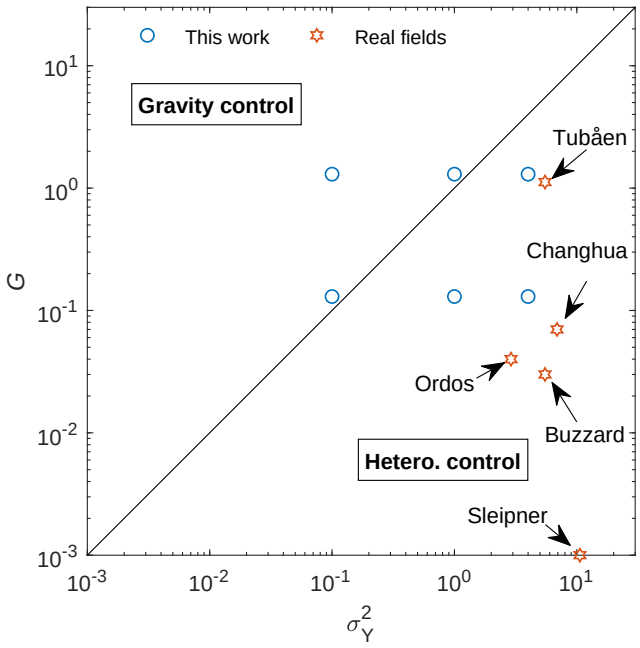

Figure 9: $\sigma_Y^2 - G$ diagram with the simulated test cases, summarized in Table 3, and the GCS field sites reviewed in Table 4.

6 Conclusions

We have investigated dissolution trapping efficiency and its uncertainty during Geological Carbon Sequestration (GCS) in randomly stratified saline formations through a set of Monte Carlo two-phase flow compositional simulations involving the dissolution of CO_2 into brine and evaporation of water into the CO_2-rich phase under different degrees of heterogeneity and gravity factors. Simulation results have provided a statistical description of dissolution efficiency as well as an examination of the impact of upscaling the permeability in numerical models. The following main findings are highlighted:

1. The interplay between heterogeneity and buoyant forces are shown to control the behavior of CO_2 migration and therefore dissolution efficiency. When buoyant forces G are relatively small compared to the degree of heterogeneity σ_Y^2, lateral CO_2 migration through high permeability layers dominates the overall behavior and dissolution efficiency increases with σ_Y^2 due to the stretching of the CO_2 plume that enhances mixing. In contrast, when buoyant forces dominate, CO_2 vertical segregation controls the behavior, diminishing the influence of heterogeneity on dissolution. A tentative behavior diagram is proposed with a transition line approximately given by $G = \sigma_Y^2$.
2. The temporal evolution of dissolution efficiency is shown to exhibit two clear regimes characterized by the characteristic segregation time t_c. Dissolution efficiency declines with time until the CO_2 gas phase rises to the top of the formation and segregates from the brine phase. After this, when $t \gg t_c$, CO_2 is forced to move laterally (viscosity forces dominate) and dissolution efficiency reaches an almost asymptotic value.
3. We have shown that the upscaling of permeability leads to an underestimation of the dissolution efficiency. This effect is more pronounced in highly heterogeneous systems with small gravity effects ($G < \sigma_Y^2$) due to the fact that lateral finger-like CO_2 plume is generated in this case following the stratification. On the contrary, when

$G > \sigma_Y^2$, a single compact $CO_2(g)$ plume floats to the upper portion of the formation regardless of heterogeneity, and upscaling is not significantly affected.

4. We have shown that most GCS field sites operate under $G \ll \sigma_Y^2$, meaning that heterogeneity typically controls dissolution efficiency in real field settings. Knowing that most numerical models that simulate CO_2 dissolution cannot properly represent the small-scale heterogeneity due to an unfeasible discretization of the domain, our results suggest that dissolution efficiency can be underestimated by a factor close to 1.5.

Acknowledgments

We acknowledge the help from Oriol Bertran-Oller and Rodrigo Perez in accessing the TITANI- high performance green computing cluster of the civil engineering school. We also acknowledge the help from Jan M. Nordbotten for sharing the code for the theoretical solution. This work was partially supported by the European Commission, through project MARSOLUT (grant H2020-MSCA-ITN-2018); by the Spanish Ministry of Economy and Competitiveness, through project MONOPOLIOS (RTI 2018-101990-B-100, MINECO/ FEDER); and by the Catalan Agency for Management of University and Research Grants through FI 2017 (EMC/2199/2017).

A Equilibrium Constants, Fugacity and Activity

The equilibrium constants of the two reaction equations are calculated as

$$K^{\beta} = K^{\beta_0} \exp \frac{\left(p_l - p^0\right) \overline{V}_{\beta}}{RT_c}, \tag{A.1}$$

with

$$K^{\beta_0} = 10^{a_{\beta} + b_{\beta} T_c + c_{\beta} T_c^2 + d_{\beta} T_c^3}, \tag{A.2}$$

where, p^0 is the reference pressure (equal to 1 bar), T_c is temperature in °C, $\overline{V}_{\beta}$ $[cm^3 \cdot mol^{-1}]$ denotes the mean molar volume of pure condensed species β when pressure change from p^0 to p_l. Here, we assume $\overline{V}_{\beta}$ is a constant. The parameters for Equation A.2, given in *Spycher et al.* [2003], are listed in Table A.1.

Table A.1: Parameters for equilibrium constants.

β	a_{β}	b_{β}	c_{β}	d_{β}	$\overline{V}_{\beta}$ [$\mathrm{cm^3 \cdot mol^{-1}}$]
$H_2O_{(g)}$	−2.209	3.097×10^{-2}	-1.098×10^{-4}	2.048×10^{-7}	18.1
$CO_{2(g)}$	1.189	1.304×10^{-2}	-5.446×10^{-5}	0	32.6

The fugacity and activity are calculated as

$$f_g^{\beta} = F^{\beta} x_g^{\beta} \frac{p_g}{p^0}, \tag{A.3}$$

$$a_l^H = x_l^H = 1 - x_l^S - x_l^C, \tag{A.4}$$

$$a_l^C = \gamma'_C m_l^C, \tag{A.5}$$

where F^β is the fugacity coefficient, x_α^β is the molar fraction of the β chemical component in the α phase, γ'_C is the activity coefficient of $CO_2(aq)$ in the liquid phase, and m_l^C is the molality of $CO_2(aq)$ in the liquid phase. Here, the simplified model for water activity, given in Equation (A.4), yields very similar results as the sophisticated Helgeson-Kirkham-Flowers (HKF) model (comparison is not shown). In order to solve Equations (A.3) to (A.5), we need to know the fugacity coefficients $F^{H,C}$ and activity coefficient γ'_C. According to *Spycher et al.* [2003], the fugacity coefficients of the gaseous species are calculated as

$$\begin{aligned}\ln F^\beta = &\ln \frac{V}{V-\mathsf{b}^{mix}} + \frac{\mathsf{b}^\beta}{V-\mathsf{b}^{mix}} - \ln\frac{V+\mathsf{b}^{mix}}{V}\frac{2}{RT_k^{1.5}\mathsf{b}^{mix}}\sum_{\beta'=C,H}\left(x_g^\beta \mathsf{a}^{\beta'-\beta}\right)\\ &+\frac{\mathsf{a}^{mix}-\mathsf{b}^\beta}{RT_k^{1.5}\left(\mathsf{b}^{mix}\right)^2}\left(\ln\frac{V+\mathsf{b}^{mix}}{V}-\frac{\mathsf{b}^{mix}}{V+\mathsf{b}^{mix}}\right)-\ln\frac{p_g V}{RT_k},\end{aligned} \tag{A.6}$$

where $\beta = (C, H, mix)$ represents the species CO_2, H_2O and $CO_2 - H_2O$ mixture, respectively, V is obtained from Equation (A.7). Assuming infinity dilution, $\mathsf{a}^{mix} = \mathsf{a}^C$ and $\mathsf{b}^{mix} = \mathsf{b}^C$. a^C and b^C are defined by (A.8) and (A.9), respectively. $\mathsf{b}^H = 1.818\times10^{-5}$ [$m^3{\cdot}mol^{-1}$] and $\mathsf{a}^{H-C} = 7.89$ [$Pa{\cdot}m^6{\cdot}K^{0.5}{\cdot}mol^{-2}$]. We assume infinite dilution of water vapor, i.e., x_g^H=0. So, we do not need a^H. The molar volume of CO_2 phase (V [$m^3{\cdot}mol^{-1}$]) is obtained by solving the cubic form of Redlich-Kwong equation [*Redlich and Kwong*, 1949],

$$V^3 - V^2\left(\frac{RT_k}{p_g}\right) - V\left(\frac{RT_k\mathsf{b}}{p_g} - \frac{\mathsf{a}}{p_g T_k^{0.5}} + \mathsf{b}^2\right) - \left(\frac{\mathsf{ab}}{p_g T_k^{0.5}}\right) = 0, \tag{A.7}$$

where a [$bar{\cdot}cm^6{\cdot}\ K^{0.5}{\cdot}mol^{-2}$] and b [$cm^3{\cdot}mol^{-1}$] are, respectively, the intermolecular attraction and repulsion of the CO_2-rich phase. For simplification, assuming infinite dilution of water vapor, we use the intermolecular attraction and repulsion of pure CO_2, a^C and b^C, to represent a and b. This is reasonable because the fraction of water vapor in the CO_2 rich phase is usually less than 1%. Therefore, according to *Spycher et al.* [2003], we have

$$\mathsf{a} = \mathsf{a}^C = 7.54\times10^7 - 4.13\times10^4 T_k, \tag{A.8}$$

and

$$\mathsf{b} = \mathsf{b}^C = 27.8. \tag{A.9}$$

Here, we note that Equation (A.7) may have more than one real solutions. The selection of the value depends on which phase –gas or liquid-is more stable. If the more stable phase is gas then we choose the maximum value. Otherwise, we choose the minimum value. To determine which phase is more stable, we need to calculate two works (w_1 and w_2) for phase transition,

$$w_1 = p_g\left(V_{max} - V_{min}\right), \tag{A.10}$$

and

$$w_2 = RT\ln\frac{V_{max}-\mathsf{b}}{V_{min}-\mathsf{b}} + \frac{\mathsf{a}}{T^{0.5}\mathsf{b}}\ln\frac{\left(V_{max}+\mathsf{b}\right)V_{min}}{\left(V_{min}+\mathsf{b}\right)V_{max}}, \tag{A.11}$$

If $w_2 \geq w_1$, then gaseous state is more stable and we choose V_{max}. Otherwise, we take V_{min}. The activity coefficient of aqueous CO_2 (γ'_C), given by *Duan and Sun* [2003], is estimated as

$$\gamma'_C = 2\lambda\left(m_l^{Na} + m_l^K + 2m_l^{Mg}\right) + \xi m_{Cl}\left(m_l^{Na} + m_l^K + m_l^{Ca} + m_l^{Mg}\right) - 0.07 m_l^{SO_4}, \tag{A.12}$$

where

$$\begin{aligned}\lambda = &- 0.411370585 + 6.07632013^{-4}T_k + \frac{97.5347708}{T_k} - \frac{0.0237622469\ p_l}{T_k} \times 10^{-5} \\ &+ \frac{0.0170656236\ p_l}{630 - T_k} \times 10^{-5} + 1.41335834 \times 10^{-5} T_k \ln\left(p_l \times 10^{-5}\right)\end{aligned} \tag{A.13}$$

and

$$\begin{aligned}\xi = &3.36389723 \times 10^{-4} - 1.98298980 \times 10^{-5} T_k + \frac{2.12220830 \times 10^{-3}\ p_l}{T_k} \times 10^{-5} \\ &- \frac{5.24873303 \times 10^{-3}\ p_l}{630 - T_k} \times 10^{-5}.\end{aligned} \tag{A.14}$$

Here, p_l is in Pa and T_k is in K. We note that this activity coefficient is not a *true* coefficient but a coefficient defined as the ratio of molality of $CO_2(aq)$ in pure water ($m_l^{C_0}$) to molality of CO_2 in brine (m_l^C) at same temperature and pressure,

$$\gamma'_{CO_2} = m_l^{C_0} / m_l^C. \tag{A.15}$$

B *Spycher and Pruess* [2005] Model for Mutual Solubility

The chemical reactions (1) and (2) are solved with the *Spycher and Pruess* [2005] model, which can calculate the mutual solubility between gas and high-salinity brine at high pressures and reservoir temperatures. *Spycher and Pruess* [2005] model is given as follows. When reaction is at equilibrium we have

$$x_g^H = \frac{K^H a_l^H}{F^H p_g} \tag{B.1}$$

and

$$x_l^C = \frac{F^C\left(1 - x_g^H\right) p_g}{55.508 \gamma'_{CO_2} K^C}. \tag{B.2}$$

Setting

$$A = \frac{K^H}{F^H p_g} \tag{B.3}$$

and

$$B = \frac{K^C p_g}{55.508 \gamma'_{CO_2} K^C}, \tag{B.4}$$

the mutual solubilities are then explicitly given as

$$x_g^H = \frac{1 - B - x_l^S}{\frac{1}{A} - B} \tag{B.5}$$

and

$$x_l^C = B\left(1 - x_g^H\right). \tag{B.6}$$

It is better to use salt molality instead of mole fraction because salt morality is independent of CO_2 solubility. Therefore, we change Equation (B.5) by

$$x_g^H = \frac{55.508(1 - B)}{\left(\frac{1}{A} - B\right)\left(\nu m_l^S + 55.508\right) + B\nu m_l^S}, \tag{B.7}$$

where ν is the stoichiometric number of ions in the salt (e.g., 2 for $NaCl$ and 3 for $MgCl_2$). The detailed derivation of Equation (B.7) can be found in *Spycher and Pruess* [2005]. With Equations (B.7) and (B.6), we can explicitly update the mole fractions in both liquid brine and gaseous CO_2-rich phases. Note that in the transport equations the concentrations are given as mass fractions, while mole fractions are used to solve the mutual solubility. We can change the mole fractions into mass fractions with

$$X_g^H = \frac{18.015 x_g^H}{18.015 x_g^H + 44.01\left(1 - x_g^H\right)} \tag{B.8}$$

and

$$X_l^C = \frac{44.01 x_l^C}{18.015\left(1 - x_l^C\right)\left(1 + 0.05844 m_l^S\right) + 44.01 x_l^C}. \tag{B.9}$$

Herein, because we use the activity coefficient of $CO_2(aq)$ given by *Duan and Sun* [2003], which is not 'true' activity coefficient, we need to slightly change the aforementioned steps [*Hassanzadeh et al.*, 2008].

C Numerical Discretization and Newton-Raphson Iteration

The governing equations (3) and (4) are discretized in space with the finite difference method. Time is discretized with fully implicit method. The discretization form is given as

$$\begin{aligned}\mathcal{F}_{1,2} =& V_c \cdot \sum_{\alpha=l,g}\left[\frac{(\phi S_\alpha \rho_\alpha X_\alpha^{H,C})^{t+\Delta t} - (\phi S_\alpha \rho_\alpha X_\alpha^{H,C})^t}{\Delta t}\right] \\ &+ \left[\sum_i\left(\mathcal{S}_i \cdot \sum_{\alpha=l,g}(\rho_\alpha X_\alpha^{H,C} \boldsymbol{q}_\alpha)^{t+\Delta t}\right) - \sum_i\left(\mathcal{S}_i \cdot \sum_{\alpha=l,g}(\phi S_\alpha \boldsymbol{D}_\alpha \rho_\alpha \nabla X_\alpha^{H,C})^{t+\Delta t}\right)\right] \\ &- \left(Q_g^{H,C}\right)^{t+\Delta t},\end{aligned} \tag{C.1}$$

where V_c is the volume the grid, $\mathcal{S}_i$ is the ith surface of the grid, and Δt is the time step. The flux $\boldsymbol{q}_\alpha$ is calculated with the two-point approximation of Darcy's law, and the upwind

method is used to calculate fluid property [*Lie*, 2019]. We then write the governing equations in compact form,

$$\boldsymbol{\mathcal{F}}(\boldsymbol{x}) = \boldsymbol{0}, \tag{C.2}$$

where

$$[\boldsymbol{\mathcal{F}}] = \begin{bmatrix} \boldsymbol{\mathcal{F}}_1 \\ \boldsymbol{\mathcal{F}}_2 \\ \boldsymbol{\mathcal{F}}_W \end{bmatrix}, \; [\boldsymbol{x}] = \begin{bmatrix} \boldsymbol{p}_l \\ \boldsymbol{p}_g \\ \boldsymbol{p}_{bh} \end{bmatrix}. \tag{C.3}$$

Here, $\mathcal{F}_W$ expresses the mass balance at the injection well, which is written as

$$0 = \mathcal{F}_W = \left(\sum_{n \in N_{well}} Q^C_{g,n} + Q^H_{g,n} \right) - Q_{well}. \tag{C.4}$$

From this, the Newton-Raphson algorithm is written as

$$\frac{\partial [\boldsymbol{\mathcal{F}}]^{t+\Delta t,k}}{\partial \boldsymbol{x}} [\delta \boldsymbol{x}]^{t+\Delta t,k} = -[\boldsymbol{\mathcal{F}}]^{t+\Delta t,k}, \tag{C.5}$$

where the superscript k denotes the iteration step, and the Jacobian matrix is

$$\left[\frac{\partial \boldsymbol{\mathcal{F}}}{\partial \boldsymbol{x}} \right]^{t+\Delta t,k} = \begin{bmatrix} \frac{\partial \boldsymbol{\mathcal{F}}_1}{\partial \boldsymbol{p}_l} & \frac{\partial \boldsymbol{\mathcal{F}}_1}{\partial \boldsymbol{p}_g} & \frac{\partial \boldsymbol{\mathcal{F}}_1}{\partial \boldsymbol{p}_{bh}} \\ \frac{\partial \boldsymbol{\mathcal{F}}_2}{\partial \boldsymbol{p}_l} & \frac{\partial \boldsymbol{\mathcal{F}}_2}{\partial \boldsymbol{p}_g} & \frac{\partial \boldsymbol{\mathcal{F}}_2}{\partial \boldsymbol{p}_{bh}} \\ \frac{\partial \boldsymbol{\mathcal{F}}_W}{\partial \boldsymbol{p}_l} & \frac{\partial \boldsymbol{\mathcal{F}}_W}{\partial \boldsymbol{p}_g} & \frac{\partial \boldsymbol{\mathcal{F}}_W}{\partial \boldsymbol{p}_{bh}} \end{bmatrix}^{t+\Delta t,k} = \begin{bmatrix} \boldsymbol{M}_{11} & \boldsymbol{M}_{12} & \boldsymbol{M}_{1W} \\ \boldsymbol{M}_{21} & \boldsymbol{M}_{22} & \boldsymbol{M}_{2W} \\ \boldsymbol{M}_{W1} & \boldsymbol{M}_{W2} & \boldsymbol{M}_{WW} \end{bmatrix}^{t+\Delta t,k} = \boldsymbol{M}^{t+\Delta t,k}. \tag{C.6}$$

Having obtained $[\delta \boldsymbol{x}]^{t+\Delta t,k}$ with Equation (C.5), we can update $[\boldsymbol{x}]^{t+\Delta t,k}$ according to

$$[\boldsymbol{x}]^{t+\Delta t,k+1} = [\boldsymbol{x}]^{t+\Delta t,k} + [\delta \boldsymbol{x}]^{t+\Delta t,k}. \tag{C.7}$$

The Newton-Raphson iteration is terminated if the maximum change of the gas and liquid pressures is smaller than the tolerance value ϵ_p ($\sim 10^{-5}$ pa), or if the maximum error is smaller than the tolerance value ϵ_{err} ($\sim 10^{-12}$). The time step is reduced to a very small value (e.g., 0.1 second) if the Newton-Raphson iteration does not converge at maximum allowed number of iteration N_{kmax}.

References

Al-Khdheeawi, E. A., S. Vialle, A. Barifcani, M. Sarmadivaleh, and S. Iglauer (2017), Influence of co2-wettability on co2 migration and trapping capacity in deep saline aquifers, *Greenhouse Gases: Science and Technology*, *7*(2), 328–338.

Angelini, O., C. Chavant, E. Chénier, R. Eymard, and S. Granet (2011), Finite volume approximation of a diffusion-dissolution model and application to nuclear waste storage, in *Mathematics and Computers in Simulation*, doi:10.1016/j.matcom.2010.12.016.

Arts, R., A. Chadwick, O. Eiken, S. Thibeau, and S. Nooner (2008), Ten years' experience of monitoring co2 injection in the utsira sand at sleipner, offshore norway, *First break*, *26*(1).

Bachu, S., D. Bonijoly, J. Bradshaw, R. Burruss, S. Holloway, N. P. Christensen, and O. M. Mathiassen (2007), Co2 storage capacity estimation: Methodology and gaps, *International Journal of Greenhouse Gas Control*, *1*(4), 430 – 443, doi:https://doi.org/10.1016/S1750-5836(07)00086-2.

Bandara, U. C., A. M. Tartakovsky, and B. J. Palmer (2011), Pore-scale study of capillary trapping mechanism during CO2 injection in geological formations, *International Journal of Greenhouse Gas Control*, doi:10.1016/j.ijggc.2011.08.014.

Birkholzer, J. T., Q. Zhou, and C. F. Tsang (2009), Large-scale impact of CO2 storage in deep saline aquifers: A sensitivity study on pressure response in stratified systems, *International Journal of Greenhouse Gas Control*, doi:10.1016/j.ijggc.2008.08.002.

Bourgeat, A., M. Jurak, and F. Smai (2010), Modelling and numerical simulation of gas migration in a nuclear waste repository.

Bryant, S. L., S. Lakshminarasimhan, and G. A. Pope (2008), Buoyancy-dominated multiphase flow and its effect on geological sequestration of CO2, *SPE Journal*, doi:10.2118/99938-PA.

Chadwick, R., and D. Noy (2010a), History-matching flow simulations and time-lapse seismic data from the sleipner co2 plume, in *Geological Society, London, petroleum geology conference series*, vol. 7, pp. 1171–1182, Geological Society of London.

Chadwick, R. A., and D. J. Noy (2010b), History-matching flow simulations and time-lapse seismic data from the Sleipner CO2 plume, in *Petroleum Geology Conference Proceedings*, doi:10.1144/0071171.

Chadwick, R. A., R. Arts, O. Eiken, G. A. Kirby, E. Lindeberg, and P. Zweigel (2004), 4D Seismic Imaging of an Injected C02 Plume at the Sleipner Field, Central North Sea, *Geological Society Memoir*, doi:10.1144/GSL.MEM.2004.029.01.29.

Chadwick, R. A., R. Arts, and O. Eiken (2005), 4D seismic quantification of a growing CO2 plume at Sleipner, North Sea, in *Petroleum Geology Conference Proceedings*, doi:10.1144/0061385.

Cottin, C., H. Bodiguel, and A. Colin (2010), Drainage in two-dimensional porous media: From capillary fingering to viscous flow, *Physical Review E - Statistical, Nonlinear, and Soft Matter Physics*, doi:10.1103/PhysRevE.82.046315.

Dentz, M., T. Le Borgne, A. Englert, and B. Bijeljic (2011), Mixing, spreading and reaction in heterogeneous media: A brief review, doi:10.1016/j.jconhyd.2010.05.002.

Doughty, C., and K. Pruess (2004), Modeling Supercritical Carbon Dioxide Injection in Heterogeneous Porous Media, *Vadose Zone Journal*, doi:10.2113/3.3.837.

Doughty, C., K. Pruess, S. M. Benson, S. D. Hovorka, P. R. Knox, and C. T. Green (2001), Capacity investigation of brine-bearing sands of the frio formation for geologic sequestration of co2, *GCCC Texts and Reports*.

Duan, Z., and R. Sun (2003), An improved model calculating CO 2 solubility in pure water and aqueous NaCl solutions from 273 to 533 K and from 0 to 2000 bar, *Chemical Geology*, doi:10.1016/S0009-2541(02)00263-2.

Ern, A., and I. Mozolevski (2012), Discontinuous Galerkin method for two-component liquid-gas porous media flows, *Computational Geosciences*, doi:10.1007/s10596-012-9277-3.

Fernàndez-Garcia, D., X. Sánchez-Vila, and A. Guadagnini (2008), Reaction rates and effective parameters in stratified aquifers, *Advances in Water Resources*, doi:10.1016/j.advwatres.2008.07.001.

Flett, M., R. Gurton, and I. Taggart (2004), The function of gas-water relative permeability hysteresis in the sequestration of carbon dioxide in saline formations, in *SPE Asia Pacific Oil and Gas Conference and Exhibition, APOGCE*, doi:10.2118/88485-ms.

Fogg, G. E., and Y. Zhang (2016), Debates-stochastic subsurface hydrology from theory to practice: A geologic perspective, *Water Resources Research*, *52*(12), 9235–9245, doi:https://doi.org/10.1002/2016WR019699.

Garcia, J. E. (2003), Fluid Dynamics of Carbon Dioxide Disposal into Saline Aquifers, *TH: Thesis (Ph.D.); Submitted to the University of California, Berkeley, CA (US); PBD: 18 Dec 2003*.

Gasda, S. E., J. M. Nordbotten, and M. A. Celia (2012), Application of simplified models to CO 2 migration and immobilization in large-scale geological systems, *International Journal of Greenhouse Gas Control*, doi:10.1016/j.ijggc.2012.03.001.

Gershenzon, N. I., R. W. Ritzi, D. F. Dominic, M. Soltanian, E. Mehnert, and R. T. Okwen (2015a), Influence of small-scale fluvial architecture on CO2 trapping processes in deep brine reservoirs, *Water Resources Research*, doi:10.1002/2015WR017638.

Gershenzon, N. I., M. Soltanian, R. W. Ritzi Jr, and D. F. Dominic (2015b), Understanding the impact of open-framework conglomerates on water–oil displacements: the victor interval of the ivishak reservoir, prudhoe bay field, alaska.

Gershenzon, N. I., M. R. Soltanian, R. W. Ritzi Jr, D. F. Dominic, D. Keefer, E. Shaffer, and B. Storsved (2015c), How does the connectivity of open-framework conglomerates within multi-scale hierarchical fluvial architecture affect oil-sweep efficiency in waterflooding?, *Geosphere*, *11*(6), 2049–2066.

Goodman, A., G. Bromhal, B. Strazisar, T. Rodosta, W. F. Guthrie, D. Allen, and G. Guthrie (2013), Comparison of methods for geologic storage of carbon dioxide in saline formations, *International Journal of Greenhouse Gas Control*, *18*, 329–342.

Green, C. P., and J. Ennis-King (2010), Effect of vertical heterogeneity on long-term migration of CO2 in saline formations, *Transport in Porous Media*, doi:10.1007/s11242-009-9498-7.

Gregersen, U. (1998), Upper Cenozoic channels and fans on 3D seismic data in the northern Norwegian North Sea, *Petroleum Geoscience*, doi:10.1144/petgeo.4.1.67.

Grude, S., M. Landrø, and B. Osdal (2013), Time-lapse pressure–saturation discrimination for co2 storage at the snøhvit field, *International Journal of Greenhouse Gas Control*, *19*, 369–378.

Gunter, W. D., S. Bachu, and S. Benson (2004), The role of hydrogeological and geochemical trapping in sedimentary basins for secure geological storage of carbon dioxide, *Geological Society, London, Special Publications*, *233*(1), 129–145.

Hassanzadeh, H., M. Pooladi-Darvish, A. M. Elsharkawy, D. W. Keith, and Y. Leonenko (2008), Predicting PVT data for CO2-brine mixtures for black-oil simulation of CO2 geological storage, *International Journal of Greenhouse Gas Control*, doi:10.1016/S1750-5836(07)00010-2.

Hayek, M., E. Mouche, and C. Mügler (2009), Modeling vertical stratification of CO2 injected into a deep layered aquifer, *Advances in Water Resources*, doi:10.1016/j.advwatres.2008.12.009.

Henri, C. V., D. Fernàndez-Garcia, and F. P. J. de Barros (2015), Probabilistic human health risk assessment of degradation-related chemical mixtures in heterogeneous aquifers: Risk statistics, hot spots, and preferential channels, *Water Resources Research*, *51*(6), 4086–4108, doi:10.1002/2014WR016717.

Humez, P., P. Audigane, J. Lions, C. Chiaberge, and G. Bellenfant (2011), Modeling of CO2 Leakage up Through an Abandoned Well from Deep Saline Aquifer to Shallow Fresh Groundwaters, *Transport in Porous Media*, doi:10.1007/s11242-011-9801-2.

Ide, S. T., K. Jessen, and F. M. Orr Jr (2007), Storage of co2 in saline aquifers: Effects of gravity, viscous, and capillary forces on amount and timing of trapping, *International Journal of Greenhouse Gas Control*, *1*(4), 481–491.

IPCC (2005), Underground Geologic Storage (Chapter 5), in *IPCC Special Report on Carbon Dioxide Capture and Storage*.

IPCC (2008), Climate change 2007: mitigation of climate change: contribution of Working Group III to the Fourth Assessment Report of the Intergovernmental Panel on Climate Change, *Choice Reviews Online*, doi:10.5860/choice.45-5006.

Jing, J., Z. Tang, Y. Yang, and L. Ma (2019), Impact of formation slope and fault on co2 storage efficiency and containment at the shenhua co2 geological storage site in the ordos basin, china, *International Journal of Greenhouse Gas Control*, *88*, 209–225.

Journel, A., and C. Huijbregts (1976), Mining geostatistics.

Juanes, R., E. J. Spiteri, F. M. Orr, and M. J. Blunt (2006), Impact of relative permeability hysteresis on geological CO2 storage, *Water Resources Research*, doi:10.1029/2005WR004806.

Kabera, T., and Y. Li (2011), Impact of co2 injection in deep saline aquifers: A study on pressure evolution in stratified formation of qianjiang sag, china, *International Journal of Chemical Engineering and Applications*, *2*(2), 121.

Knudby, C., and J. Carrera (2005), On the relationship between indicators of geostatistical, flow and transport connectivity, *Advances in Water Resources*, *28*(4), 405 – 421, doi:https://doi.org/10.1016/j.advwatres.2004.09.001.

Krevor, S., M. J. Blunt, S. M. Benson, C. H. Pentland, C. Reynolds, A. Al-Menhali, and B. Niu (2015), Capillary trapping for geologic carbon dioxide storage - From pore scale physics to field scale implications, *International Journal of Greenhouse Gas Control*, doi:10.1016/j.ijggc.2015.04.006.

Krevor, S. C., R. Pini, B. Li, and S. M. Benson (2011), Capillary heterogeneity trapping of CO2 in a sandstone rock at reservoir conditions, *Geophysical Research Letters*, doi:10.1029/2011GL048239.

Kumar, A., R. Ozah, M. Noh, G. A. Pope, S. Bryant, K. Sepehmoori, and L. W. Lake (2005), Reservoir simulation of CO2 storage in deep saline aquifers, *SPE Journal*, doi:10.2118/89343-pa.

Leal, A. M., M. J. Blunt, and T. C. LaForce (2013), A robust and efficient numerical method for multiphase equilibrium calculations: Application to CO2-brine-rock systems at high temperatures, pressures and salinities, *Advances in Water Resources*, doi:10.1016/j.advwatres.2013.02.006.

Lee, Y., K. Kim, W. Sung, and I. Yoo (2010), Analysis of the leakage possibility of injected CO2 in a saline aquifer, *Energy and Fuels*, doi:10.1021/ef100073m.

Lenormand, R., E. Touboul, and C. Zarcone (1988), Numerical models and experiments on immiscible displacements in porous media, *Journal of Fluid Mechanics*, doi:10.1017/S0022112088000953.

Li, D., Y. He, H. Zhang, W. Xu, and X. Jiang (2017), A numerical study of the impurity effects on co2 geological storage in layered formation, *Applied energy*, *199*, 107–120.

Li, D., H. Zhang, Y. Li, W. Xu, and X. Jiang (2018), Effects of n2 and h2s binary impurities on co2 geological storage in stratified formation–a sensitivity study, *Applied energy*, *229*, 482–492.

Lie, K.-A. (2019), *An introduction to reservoir simulation using MATLAB/GNU Octave: User guide for the MATLAB Reservoir Simulation Toolbox (MRST)*, Cambridge University Press.

Maldal, T., and I. Tappel (2004), Co2 underground storage for snøhvit gas field development, *Energy*, *29*(9-10), 1403–1411.

Mathieson, A., I. Wright, D. Roberts, and P. Ringrose (2009), Satellite imaging to monitor co2 movement at krechba, algeria, *Energy Procedia*, *1*(1), 2201–2209.

Mathieson, A., J. Midgely, I. Wright, N. Saoula, and P. Ringrose (2011), In salah co2 storage jip: Co2 sequestration monitoring and verification technologies applied at krechba, algeria, *Energy Procedia*, *4*, 3596–3603.

McGuire, P., A. Spence, F. Stalkup, M. Cooley, et al. (1995), Core acquisition and analysis for optimization of the prudhoe bay miscible-gas project, *SPE reservoir engineering*, *10*(02), 94–100.

Michael, K., A. Golab, V. Shulakova, J. Ennis-King, G. Allinson, S. Sharma, and T. Aiken (2010), Geological storage of co2 in saline aquifers—a review of the experience from existing storage operations, *International journal of greenhouse gas control*, *4*(4), 659–667.

Mori, H., T. Sakaki, and T. H. Illangasekare (2015), Laboratory study of geological carbon sequestration using surrogate fluids: Dielectric measurement and scaling of capillary pressure-saturation relationships, *International Journal of Greenhouse Gas Control*, doi:10.1016/j.ijggc.2015.01.023.

Mouche, E., M. Hayek, and C. Mügler (2010), Upscaling of CO2 vertical migration through a periodic layered porous medium: The capillary-free and capillary-dominant cases, *Advances in Water Resources*, doi:10.1016/j.advwatres.2010.07.005.

Neumann, R., P. Bastian, and O. Ippisch (2013), Modeling and simulation of two-phase two-component flow with disappearing nonwetting phase, *Computational Geosciences*, *17*(1), 139–149, doi:10.1007/s10596-012-9321-3.

Nordbotten, J. M., and M. A. Celia (2006), Similarity solutions for fluid injection into confined aquifers, *Journal of Fluid Mechanics*, doi:10.1017/S0022112006000802.

Obi, E.-O. I., and M. J. Blunt (2006), Streamline-based simulation of carbon dioxide storage in a north sea aquifer, *Water Resources Research*, *42*(3).

Oh, J., K. Y. Kim, W. S. Han, E. Park, and J. C. Kim (2015), Migration behavior of supercritical and liquid CO2 in a stratified system: Experiments and numerical simulations, *Water Resources Research*, doi:10.1002/2015WR017022.

Oldenburg, C. M., and A. P. Rinaldi (2011), Buoyancy Effects on Upward Brine Displacement Caused by CO2 Injection, *Transport in Porous Media*, doi:10.1007/s11242-010-9699-0.

Onoja, M. U., J. D. Williams, H. Vosper, and S. M. Shariatipour (2019), Effect of sedimentary heterogeneities in the sealing formation on predictive analysis of geological co2 storage, *International Journal of Greenhouse Gas Control*, *82*, 229–243.

Plampin, M. R., R. N. Lassen, T. Sakaki, M. L. Porter, R. J. Pawar, K. H. Jensen, and T. H. Illangasekare (2014), Heterogeneity-enhanced gas phase formation in shallow aquifers during leakage of CO2-saturated water from geologic sequestration sites, *Water Resources Research*, doi:10.1002/2014WR015715.

Plug, W. J., and J. Bruining (2007), Capillary pressure for the sand-CO2-water system under various pressure conditions. Application to CO2 sequestration, *Advances in Water Resources*, doi:10.1016/j.advwatres.2007.05.010.

Pruess, K., and J. Nordbotten (2011), Numerical Simulation Studies of the Long-term Evolution of a CO2 Plume in a Saline Aquifer with a Sloping Caprock, *Transport in Porous Media*, doi:10.1007/s11242-011-9729-6.

Rasmusson, K., C.-F. Tsang, Y. Tsang, M. Rasmusson, L. Pan, F. Fagerlund, J. Bensabat, and A. Niemi (2015), Distribution of injected co2 in a stratified saline reservoir accounting for coupled wellbore-reservoir flow, *Greenhouse Gases: Science and Technology*, *5*(4), 419–436.

Redlich, O., and J. N. Kwong (1949), On the thermodynamics of solutions. V. An equation of state. Fugacities of gaseous solutions, *Chemical Reviews*, doi:10.1021/cr60137a013.

Renard, P., and G. de Marsily (1997), Calculating equivalent permeability: a review, *Advances in Water Resources*, *20*(5), 253–278, doi:https://doi.org/10.1016/S0309-1708(96)00050-4.

Riaz, A., M. HESSE, H. A. TCHELEPI, and F. M. ORR (2006), Onset of convection in a gravitationally unstable diffusive boundary layer in porous media, *Journal of Fluid Mechanics*, *548*, 87–111, doi:10.1017/S0022112005007494.

Saaltink, M. W., V. Vilarrasa, F. De Gaspari, O. Silva, J. Carrera, and T. S. Rötting (2013), A method for incorporating equilibrium chemical reactions into multiphase flow models for co2 storage, *Advances in Water Resources*, *62*, 431 – 441, doi:https://doi.org/10.1016/j.advwatres.2013.09.013, computational Methods in Geologic CO2 Sequestration.

Sanchez-Vila, X., A. Guadagnini, and J. Carrera (2006), Representative hydraulic conductivities in saturated groundwater flow, *Reviews of Geophysics*, *44*(3), doi:https://doi.org/10.1029/2005RG000169.

Schwartz, M. O. (2014), Modelling leakage and groundwater pollution in a hypothetical co2 sequestration project, *International Journal of Greenhouse Gas Control*, *23*, 72–85.

Silin, D., T. Patzek, and S. M. Benson (2009), A model of buoyancy-driven two-phase countercurrent fluid flow, *Transport in Porous Media*, *76*(3), 449–469.

Spycher, N., and K. Pruess (2005), CO2-H2O mixtures in the geological sequestration of CO2. II. Partitioning in chloride brines at 12-100°C and up to 600 bar, *Geochimica et Cosmochimica Acta*, doi:10.1016/j.gca.2005.01.015.

Spycher, N., K. Pruess, and J. Ennis-King (2003), CO2-H2O mixtures in the geological sequestration of CO2. I. Assessment and calculation of mutual solubilities from 12 to 100°C

and up to 600 bar, *Geochimica et Cosmochimica Acta*, doi:10.1016/S0016-7037(03)00273-4.

Stalkup, F., and S. Crane (1994), Reservoir description detail required to predict solvent and water saturations at an observation well, *SPE Reservoir Engineering*, *9*(01), 35–43.

Strandli, C. W., and S. M. Benson (2013), Identifying diagnostics for reservoir structure and CO2 plume migration from multilevel pressure measurements, *Water Resources Research*, doi:10.1002/wrcr.20285.

Sung, R.-T., M.-H. Li, J.-J. Dong, A. T.-S. Lin, S.-K. Hsu, C.-Y. Wang, and C.-N. Yang (2014), Numerical assessment of co2 geological sequestration in sloping and layered heterogeneous formations: A case study from taiwan, *International Journal of Greenhouse Gas Control*, *20*, 168–179.

Szulczewski, M. L., C. W. MacMinn, H. J. Herzog, and R. Juanes (2012), Lifetime of carbon capture and storage as a climate-change mitigation technology, *Proceedings of the National Academy of Sciences*, *109*(14), 5185–5189.

Trevisan, L., A. Cihan, F. Fagerlund, E. Agartan, H. Mori, J. T. Birkholzer, Q. Zhou, and T. H. Illangasekare (2014), Investigation of mechanisms of supercritical CO2 trapping in deep saline reservoirs using surrogate fluids at ambient laboratory conditions, *International Journal of Greenhouse Gas Control*, doi:10.1016/j.ijggc.2014.07.012.

Trevisan, L., R. Pini, A. Cihan, J. T. Birkholzer, Q. Zhou, and T. H. Illangasekare (2015), Experimental analysis of spatial correlation effects on capillary trapping of supercritical CO2 at the intermediate laboratory scale in heterogeneous porous media, *Water Resources Research*, doi:10.1002/2015WR017440.

Tsang, C.-F., Y. W. Tsang, J. Birkholzer, and L. Moreno (2001), Dynamic channeling of flow and transport in saturated and unsaturated heterogeneous media, *GEOPHYSICAL MONOGRAPH-AMERICAN GEOPHYSICAL UNION*, *42*, 33–44.

Van der Meer, L. (1995), The co2 storage efficiency of aquifers, *Energy conversion and management*, *36*(6-9), 513–518.

van Genuchten, M. T. (1980), A Closed-form Equation for Predicting the Hydraulic Conductivity of Unsaturated Soils1, *Soil Science Society of America Journal*, doi:10.2136/sssaj1980.03615995004400050002x.

Vilarrasa, V., D. Bolster, M. Dentz, S. Olivella, and J. Carrera (2010), Effects of CO2 Compressibility on CO2 Storage in Deep Saline Aquifers, *Transport in Porous Media*, doi:10.1007/s11242-010-9582-z.

Wang, K., T. Xu, H. Tian, and F. Wang (2016), Impacts of mineralogical compositions on different trapping mechanisms during long-term co2 storage in deep saline aquifers, *Acta Geotechnica*, *11*(5), 1167–1188.

Wang, Y. (2022), Numerical modeling of geological carbon sequestration: Enhanced dissolution in randomly heterogeneous media, Ph.D. thesis, Technical University of Catalonia.

Wen, X.-H., and J. Gómez-Hernández (1996), Upscaling hydraulic conductivities in heterogeneous media: An overview, *Journal of Hydrology*, *183*(1), ix–xxxii, doi:https://doi.org/10.1016/S0022-1694(96)80030-8.

Xiao, T., B. McPherson, R. Esser, W. Jia, N. Moodie, S. Chu, and S.-Y. Lee (2019), Forecasting commercial-scale co2 storage capacity in deep saline reservoirs: Case study of buzzard's bench, central utah, *Computers & Geosciences*, *126*, 41–51.

Xu, T., E. Sonnenthal, N. Spycher, and K. Pruess (2004), Toughreact user's guide: A simulation program for non-isothermal multiphase reactive geochemical transport in variable saturated geologic media, *Tech. rep.*, Lawrence Berkeley National Lab.(LBNL), Berkeley, CA (United States).

Xu, T., N. Spycher, E. Sonnenthal, G. Zhang, L. Zheng, and K. Pruess (2011), Toughreact version 2.0: A simulator for subsurface reactive transport under non-isothermal multiphase flow conditions, *Computers & Geosciences*, *37*(6), 763–774.

Zhang, M., Y. Zhang, and P. Lichtner (2017), Evaluating model complexity in simulating supercritical co2 dissolution, leakage, footprint, and reservoir pressure for three-dimensional hierarchical aquifer, *International Journal of Greenhouse Gas Control*, *64*, 284–299.

Zhao, B., C. W. MacMinn, and R. Juanes (2014), Residual trapping, solubility trapping and capillary pinning complement each other to limit co2 migration in deep saline aquifers, *Energy Procedia*, *63*, 3833–3839.

Zhou, Q., J. T. Birkholzer, C.-F. Tsang, and J. Rutqvist (2008), A method for quick assessment of co2 storage capacity in closed and semi-closed saline formations, *International Journal of Greenhouse gas control*, *2*(4), 626–639.

Zhou, Q., J. T. Birkholzer, E. Mehnert, Y.-F. Lin, and K. Zhang (2010), Modeling basin-and plume-scale processes of co2 storage for full-scale deployment, *Groundwater*, *48*(4), 494–514.

Zinn, B., and C. F. Harvey (2003), When good statistical models of aquifer heterogeneity go bad: A comparison of flow, dispersion, and mass transfer in connected and multivariate gaussian hydraulic conductivity fields, *Water Resources Research*, *39*(3), doi:10.1029/2001WR001146.

Support Information for: CO_2 Dissolution Efficiency during Geological Carbon Sequestration (GCS) in Perfectly Stratified Aquifers

Yufei Wang[1,2] **Daniel Fernàndez-Garcia**[1,2] **Maarten W. Saaltink**[1,2]

[1]Dept. of Civil and Environmental Engineering, Universitat Politècnica de Catalunya, Jordi Girona 1-3, 08034 Barcelona, Spain
[2]Associated Unit: Hydrogeology Group (UPC-CSIC)

Corresponding author: Yufei Wang, yufei.wang@upc.edu

Abstract
This support information offers the saturation and concentration distributions for different cases.

Figures

Figure 1 shows the distributions of $CO_2(g)$ plumes and $CO_2(aq)$ concentrations for the real heterogeneous field when normal injection rate is employed.

Figure 2 shows the distributions of $CO_2(g)$ plumes and $CO_2(aq)$ concentrations for the real heterogeneous field when slow injection rate is employed.

Figure 3 illustrates distributions of $CO_2(g)$ saturation and $CO_2(aq)$ concentration for the representative formations with upscaled permeability when normal injection rate is employed.

Figure 4 illustrates distributions of $CO_2(g)$ saturation and $CO_2(aq)$ concentration for the representative formations with upscaled permeability when slow injection rate is employed.

Figure 5 shows the distributions of ensemble average saturation and ensemble average concentration for heterogeneous cases when normal injection rate is employed.

Remark

The distribution of dissolved $CO_2(aq)$ concentration in brine is closely related to that of $CO_2(g)$ saturation. Therefore, in the paper we only show the distribution of $CO_2(g)$ saturation.

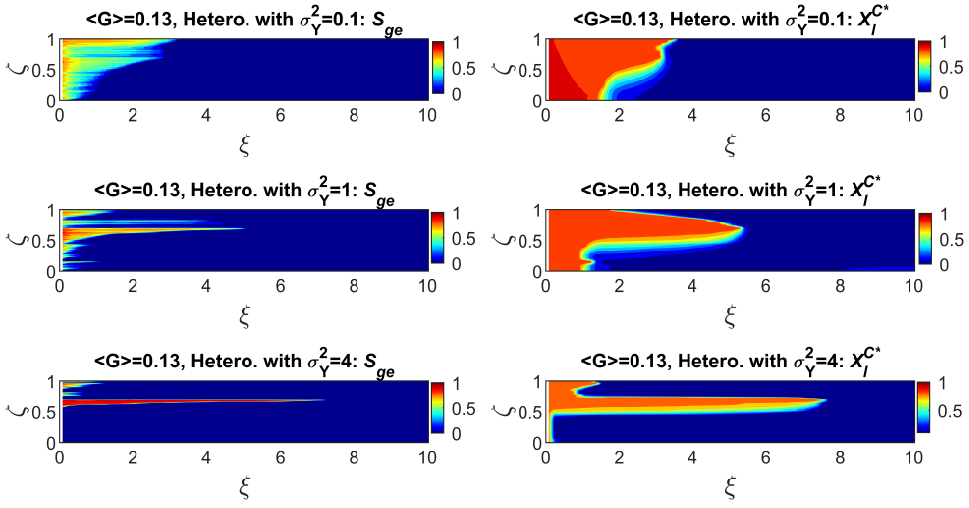

Figure 1: $CO_2(g)$ plumes (left column) and $CO_2(aq)$ concentrations in brine phase (right column) for the representative realization of the layered formations with σ_Y^2=0.1, 1, 4, respectively; normal injection rate Q_r=2.5 [Mt/year] is employed.

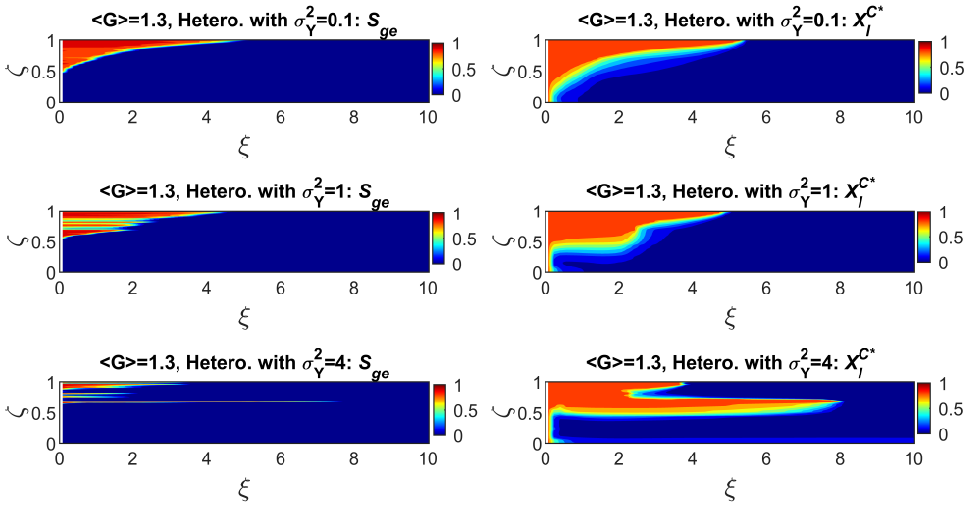

Figure 2: $CO_2(g)$ plumes (left column) and $CO_2(aq)$ concentrations in brine phase (right column) for the representative realization of the layered formations with σ_Y^2=0.1, 1, 4, respectively; slow injection rate Q_r=0.25 [Mt/year] is employed.

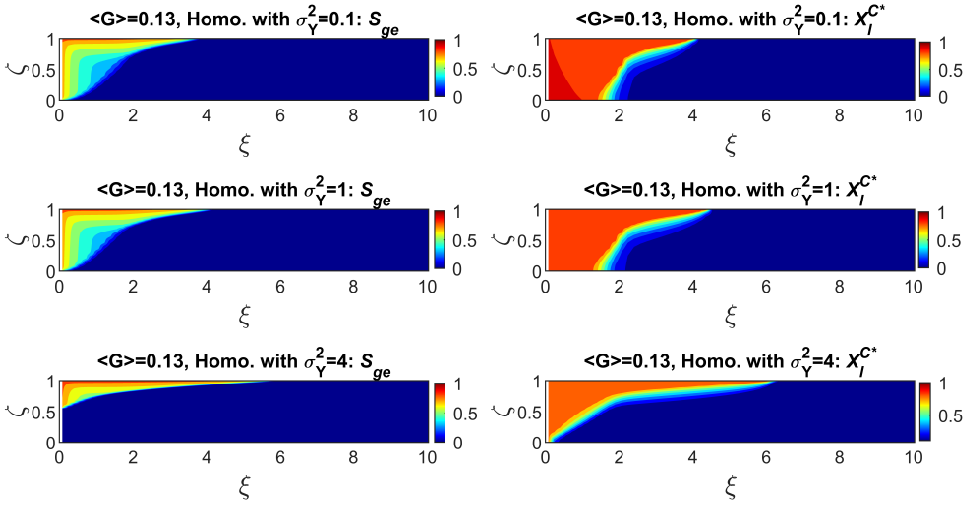

Figure 3: $CO_2(g)$ plumes (left column) and $CO_2(aq)$ concentrations in brine phase (right column) for representative formations with upscaled permeability corresponding to σ_Y^2=0.1, 1, 4, respectively; normal injection rate Q_r=2.5 [Mt/year] is employed.

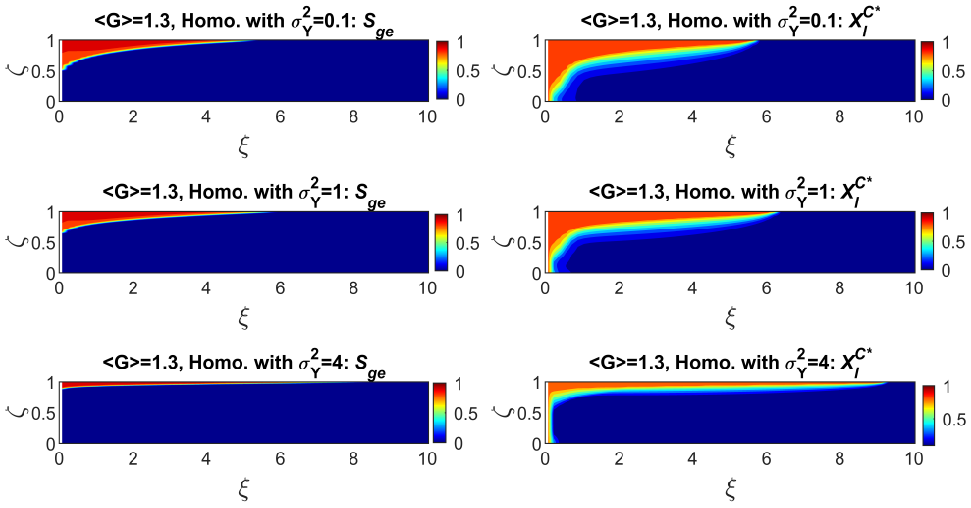

Figure 4: $CO_2(g)$ plumes (left column) and $CO_2(aq)$ concentrations in brine phase (right column) for representative formations with upscaled permeability corresponding σ_Y^2=0.1, 1, 4, respectively; slow injection rate Q_r=0.25 [Mt/year] is employed.

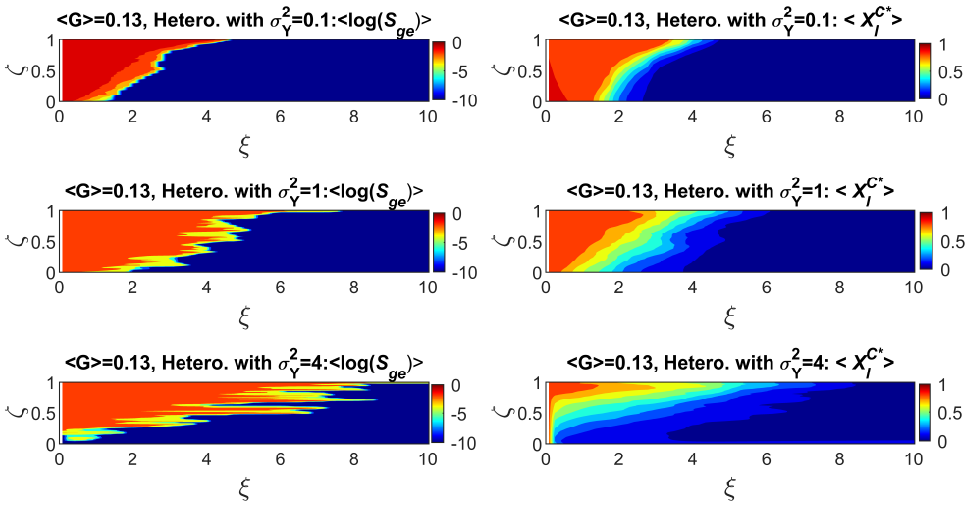

Figure 5: Ensemble averages of $CO_2(g)$ plumes (left column) and $CO_2(aq)$ concentrations in brine phase (right column) for the layered formations with σ_Y^2=0.1, 1, 4, respectively; normal injection rate Q_{well}=2.5 [Mt/year] is employed.